

A novel breast software phantom for biomechanical modeling of elastography

Syeda Naema Bhatti and Mallika Sridhar-Keralapura

Citation: *Medical Physics* **39**, 1748 (2012); doi: 10.1118/1.3690467

View online: <http://dx.doi.org/10.1118/1.3690467>

View Table of Contents: <http://scitation.aip.org/content/aapm/journal/medphys/39/4?ver=pdfcov>

Published by the [American Association of Physicists in Medicine](#)

Articles you may be interested in

[A novel shape-similarity-based elastography technique for prostate cancer assessment](#)

Med. Phys. **42**, 5110 (2015); 10.1118/1.4927572

[Silicone breast phantoms for elastographic imaging evaluation](#)

Med. Phys. **40**, 063503 (2013); 10.1118/1.4805096

[Toward in vivo lung's tissue incompressibility characterization for tumor motion modeling in radiation therapy](#)

Med. Phys. **40**, 051902 (2013); 10.1118/1.4798461

[Strain-encoded breast MRI in phantom and ex vivo specimens with histological validation: Preliminary results](#)

Med. Phys. **39**, 7710 (2012); 10.1118/1.4749963

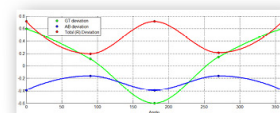
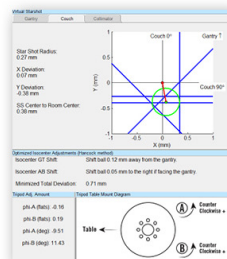
[Analytic modeling of breast elastography](#)

Med. Phys. **30**, 2340 (2003); 10.1118/1.1599953

**Achieve
Sub Millimeter
Accuracy**



- Fast and accurate EPID-based measurement of isocenter position
- Characterization of gantry, couch, and collimator rotation
- Calculates optimization of couch axis automatically
- Compatible with MLC, jaw, or cone based fields of all sizes



New - Eliminate your need for films, and increase your accuracy by using the all new Virtual Starshot, reconstructed using a set of Winston-Lutz images! US Patent 9192784

A novel breast software phantom for biomechanical modeling of elastography

Syeda Naema Bhatti^{a)} and Mallika Sridhar-Keralapura^{b)}

Biomedical Systems Lab, Department of Electrical Engineering, San Jose State University,
One Washington Square, San Jose, California 95192

(Received 13 June 2011; revised 7 February 2012; accepted for publication 12 February 2012;
published 9 March 2012)

Purpose: In developing breast imaging technologies, testing is done with phantoms. Physical phantoms are normally used but their size, shape, composition, and detail cannot be modified readily. These difficulties can be avoided by creating a software breast phantom. Researchers have created software breast phantoms using geometric and/or mathematical methods for applications like image fusion. The authors report a 3D software breast phantom that was built using a mechanical design tool, to investigate the biomechanics of *elastography* using finite element modeling (FEM). The authors propose this phantom as an intermediate assessment tool for *elastography* simulation; for use after testing with commonly used phantoms and before clinical testing. The authors design the phantom to be flexible in both, the breast geometry and biomechanical parameters, to make it a useful tool for *elastography* simulation.

Methods: The authors develop the 3D software phantom using a mechanical design tool based on illustrations of normal breast anatomy. The software phantom does not use geometric primitives or imaging data. The authors discuss how to create this phantom and how to modify it. The authors demonstrate a typical *elastography* experiment of applying a static stress to the top surface of the breast just above a simulated tumor and calculate normal strains in 3D and in 2D with plane strain approximations with linear solvers. In particular, they investigate contrast transfer efficiency (CTE) by designing a parametric study based on location, shape, and stiffness of simulated tumors. The authors also compare their findings to a commonly used *elastography* phantom.

Results: The 3D breast software phantom is flexible in shape, size, and location of tumors, glandular to fatty content, and the ductal structure. Residual modulus, maps, and profiles, served as a guide to optimize meshing of this geometrically nonlinear phantom for biomechanical modeling of *elastography*. At best, low residues (around 1–5 KPa) were found within the phantom while errors were elevated (around 10–30 KPa) at tumor and lobule boundaries. From our FEM analysis, the breast phantom generated a superior CTE in both 2D and in 3D over the block phantom. It also showed differences in CTE values and strain contrast for deep and shallow tumors and showed significant change in CTE when 3D modeling was used. These changes were not significant in the block phantom. Both phantoms, however, showed worsened CTE values for increased input tumor-background modulus contrast.

Conclusions: Block phantoms serve as a starting tool but a next level phantom, like the proposed breast phantom, will serve as a valuable intermediate for *elastography* simulation before clinical testing. Further, given the CTE metrics for the breast phantom are superior to the block phantom, and vary for tumor shape, location, and stiffness, these phantoms would enhance the study of *elastography* contrast. Further, the use of 2D phantoms with plane strain approximations overestimates the CTE value when compared to the true CTE achieved with 3D models. Thus, the use of 3D phantoms, like the breast phantom, with no approximations, will assist in more accurate estimation of modulus, especially valuable for 3D *elastography* systems. © 2012 American Association of Physicists in Medicine. [<http://dx.doi.org/10.1118/1.3690467>]

Key words: breast software phantom, elastography simulation, FEM analysis

I. INTRODUCTION

Imaging the breast is a critical component not only for breast cancer screening but also for diagnosis, treatment, and follow-up of patients with the disease. In developing such imaging technologies, a critical component is the testing media or phantoms. Physical phantoms are normally used and are created to provide a realistic realization of *in vivo* breast tissue. However, their size, shape, composition, and

detail cannot be modified readily. These difficulties, at least in early research, can be avoided by creating a software breast phantom.

Mimicking a complex anatomical structure like the breast using software is extremely challenging given its complicated arrangement of fat, glandular tissue, blood vessels, bone, and muscle, whose distribution and configuration varies from woman to woman. Creating software breast phantoms is not new. Several attempts have been made at

creating these in either 2D or 3D with different levels of anatomic detail. A phantom does not need to exactly describe all the relevant anatomy but yet can produce realistic images when modeled, when designed for a particular imaging modality and application.^{1,2}

Two types of phantoms have been reported in the literature—geometric (or mathematical) and segmented (or voxelized). Many of the initial mathematical breast models were 2D (Refs. 3 and 4) with lumped glandular areas. More recently, 3D models with the ductal network have been reported.^{5–7} In general, the focus was on creating simulated mammograms for understanding its features. For instance, Bliznakova *et al.*⁷ built a very complex model by incorporating a 3D voxel array with geometric primitives, a ductal network, and a model for lesions. Mathematical models are very flexible and quite detailed but they require clear geometric primitives and equations. These are quite complicated to setup and difficult to recreate from other studies. In the voxelized area, groups like Samani *et al.*,⁸ Li *et al.*,⁹ Hoeschen *et al.*,¹⁰ Azar *et al.*,¹¹ and Rajgopalan *et al.*² among others, took a direct route to creating a phantom by segmenting an *in vivo* CT or MRI scan of the breast into a 3D voxel volume, making the model patient specific. Such software phantoms require patient volumetric imaging data and classification algorithms, making it challenging in early phases of a project. Most of these voxelized phantoms subsequently incorporated deformable (biomechanical) models based on finite elements (FEM) to predict breast deformations for applications like registration of MRI to mammograms,¹² registration of different views of mammograms,¹ simulation of gravity loading for surgical planning,¹³ gravity and compression modeling,^{14,15} and so on.

One other interesting application of breast software phantoms would be in the field of *strain imaging*, also referred to as *elastography*,¹⁶ when static external compressions are used. In *elastography*, ultrasound or MRI data are collected synchronously when a compressive stimulus is applied to the breast. Data are then processed to map mechanical properties like strain or modulus of tissue.

FEM methods in the field of static *elastography* have primarily focused on three major areas—(a) estimation of the Young's Modulus in tissue, which if estimated accurately would provide an absolute distribution of the underlying tissue elastic properties—critically important for tumor differentiation and characterization;¹⁷ (b) mapping axial and shear strains and calculating contrast transfer efficiency (CTE) for the purpose of understanding how stiff lesions translate into observed strain patterns;^{18,19} (c) testing of types of models such as linear, pseudo-linear, and nonlinear in terms of their applicability and assumptions. For example, investigating whether large deformations applied to tissue can be approximated by a series of smaller linear isotropic deformations.²⁰ For preliminary investigation of these (a)–(c) types of studies, researchers have commonly used software phantoms that are simple in shape (rectangular or hemispherical—if modeling the breast) and homogenous with cylindrical or spherical tumors embedded.^{17,19,21,22} Sometimes, layers (fat and gland) are modeled but again they are homogeneous. Furthermore,

most of the FEM phantoms are setup in 2D or the analysis has been done in 2D with a plane stress/strain approximation on the basis that traditional *elastography* in the clinic over the past 15 years has been done using basic 2D ultrasound.

Another technology that has become popular recently is 3D *elastography* with the advent of 2D transducer arrays and faster system performance for 3D motion tracking.¹⁷ Also, beyond the ability to just create 3D images, the ability to track motion in the elevational direction would eliminate the use of just the 2D displacement field and other simplifying assumptions (like plane strain or stress) during modulus reconstruction,^{17,22} which has been shown to cause significant errors in modulus values. Beyond the simple phantoms (homogenous phantoms with inclusions), no advanced phantoms in 3D have been reported for *elastography* to investigate areas (a)–(c) discussed above.

More recently, emphasis has been placed on better phantoms for testing *elastography* systems given that success in the clinic has been variable—generally successful for larger stiff tumors and not so successful for smaller softer deeper cases.^{23–28} Madsen *et al.*²⁹ states that more closely a phantom mimics a patient, more effective is the phantom in uncovering weaknesses of the technology. He suggests creation of breast phantoms to be a valuable intermediate between simple phantoms (containing, for example, cylindrical inclusions in homogeneous backgrounds) and actual patients for assessment of *elastography* systems and further refinements in hardware or software algorithms. Creation of such phantoms, physically, would be very challenging. Hence, the area of software breast phantoms has emerged where software phantoms can be used to create any number of anatomical variations present in a patient population like size, shape, composition, and parenchymal details. Both Li *et al.*⁹ and Rajgopal *et al.*² discuss the applications of such breast phantoms in several areas like, image-guided breast biopsies, tomosynthesis, dual-energy mammography, and *elastography*. They say that it would significantly benefit from having a more accurate model of the breast to allow for better understanding and optimization of clinical scenarios.

With these aspects in mind, we chose to design a software breast phantom that is well beyond what has been reported in the *elastography* literature, to be truly three-dimensional with full regard and flexibility to breast contours, size, layers, and detail (especially in the glandular region) using a mechanical design tool such as “SOLIDWORKS.” Such a phantom could be designed with a mathematical model or with a patient's MRI or CT imaging data but we chose not to approach it from these angles due to lack of imaging data and difficulty in establishing the geometric primitives for mathematical models. This 3D breast framework/software phantom is proposed as an intermediate assessment tool for *elastography* simulation; for use after initial testing with simple commonly used phantoms (e.g., rectangular homogeneous phantom with a spherical inclusion) and before clinical testing. Physical phantoms can be created as preliminary testing tools but subsequent testing of more complicated scenarios can be done with such a software phantom.

This software phantom would be a great tool to study *elastography* as it allows flexibility in both, the choice of the breast geometry and biomechanical parameters, and has a more realistic 3D shape, size, and internal structure when compared to simple phantoms. We propose this software breast phantom to be an important addition to physical phantoms to simulate *elastography* for applications like modulus reconstruction, CTE testing, nonlinear/linear modeling, and hyperelasticity/viscoelasticity. The proposed phantom can be setup to be flexible in its modeling framework—linear modeling is demonstrated in this paper but it can be extended to hyperelastic modeling to simulate scenarios of larger compressions commonly seen in clinic, which will be a subject of future work. Such information will be extremely useful to guide clinicians in applying the right stress profile to maximize contrast to possibly obviate difficulties in imaging small, deep, less stiff tumors. In the current work, the stress profile was kept constant and comparisons were made between this phantom and a simple rectangular phantom for different tumor stiffness, shape, and location to introduce this phantom into the field of *elastography*.

In particular, we focus on the following aspects as the objectives of this paper—(1) developing a software phantom using a mechanical tool using illustrations of breast anatomy with full flexibility for the breast geometry modifications; (2) using it in *elastography*, where such sophisticated phantoms have never been used, in particular for CTE analysis. We investigate CTE, i.e., how modulus contrast (tumor vs background modulus) translates into strain contrast (that is of clinical interest) by designing a parametric study using 3D modeling (with no approximations) and with 2D slices (with plane strain approximations), all with linear methods. We also compare our software phantom to a commonly used *elastography* phantom.

Given that such a detailed breast phantom with a mechanical design tool has never been designed before to our knowledge, we detail all the design specifics in this paper. Further, since such a detailed breast model has never been used in the field of *elastography*, we illustrate its use in basic *elastography* simulation with a parametric study. Future work will involve modulus reconstruction efforts and nonlinear modeling for more complicated scenarios.

II. BREAST ANATOMY

The breast is a heterogeneous body, extending from the level of the second rib on the platysma myoides muscle, to the seventh rib on the external oblique muscle.² In terms of muscle distribution, two thirds of the bed of the breast is formed by the pectoralis fascia overlaying the pectoralis major muscle; the other third, by the fascia covering the serratus anterior muscle.³⁰ The breast is composed of glandular (secretory) and adipose (fatty) tissue, and is supported by a loose framework of fibrous connective tissue called Coopers ligaments. These ligaments provide the shape of the breast by pulling on the skin. The glandular tissue consists of lobes that are comprised of lobules containing alveoli arranged in a tree-like structure.³⁰ Ducts drain the alveoli and merge into larger ducts that eventually converge into main milk ducts.

These then dilates slightly to form the lactiferous sinus before narrowing as it passes through the nipple and open onto the nipple surface. The blood supply to the breast is provided mainly by the anterior and posterior medial branches of the internal mammary artery and the lateral mammary branch of the lateral thoracic artery. The course of the arteries is generally not associated with the ductal system of the breast. Also, there are no muscles within the breast. The pectoralis muscles lie under each breast and cover the ribs.

The ratio of glandular to adipose tissue estimated by mammography is 1:1 on average, and it is well documented that the proportion of glandular tissue declines with both advancing age and increasing breast size.³¹ Stroma is the term used for breast tissue that does not deal with milk production. Muscle tissue, connective (Cooper's) ligaments, and fatty tissue are included in this category. Breast parenchyma, along with the stroma make up the density (or the firmness) of the breast. The size and shape of the breast varies over time in the same woman because of changes during the menstrual cycle, pregnancy, lactation, and menopause.³¹ Cancers in the breast that begin in the glandular tissue are broadly termed as Adenocarcinomas. Those that originate in lobules are known as lobular carcinomas and those that begin in ducts are ductal carcinomas.

III. 3D BREAST MODEL

III.A. Breast phantom detail

Software phantom creation has been heavily governed by the application for which it is used.² What level of detail is needed is a question worth asking. The standard descriptions of the human breast are based on Coopers³² magnificent cadaver dissections of the breasts of women. However, the imaging modalities have difficulty in clearly elucidating this breast anatomy³³ if compared to the dissections. Since we are currently interested in applying our phantom to ultrasound *elastography*, we are only concerned with what the ultrasound modality can visualize in the breast. Detailed ultrasound studies on the breast have shown that main ducts^{33,34} may be visible, but glandular lobes, lobules, or alveoli do not appear clear and separated.³⁵ However, the glandular structure appears diffuse and displays high echogenicity. Strain imaging has much worse resolution than regular ultrasound (sometime 10–15 times) and clinical strain images do not show alveoli or lobular structures but show a general diffused region.²⁶ Retromammary fat (fat encasing the glandular tissue) looks quite uniform and has low echogenicity.^{34,35} A little more insight in terms of glandular and fat compartments may be obtained from an MRI image. Generally, there is clear differentiation between glandular regions and fatty regions (black vs white, respectively), but again glandular regions are diffuse with no clear demarcation between lobes, lobules, and alveoli.³⁶

We base our 3D models on the above ultrasound modality observations and concentrate mainly on making the glandular structure diffuse. Furthermore, since most tumors are located within glandular tissue, we make fat uniform and do not compartmentalize it. We construct the ductal framework (with larger ducts and lobular structures) with fat surrounding and

TABLE I. Measurements from anatomy for 3D model.

Glandular tissue (Refs. 30, 34, and 37)
Depth of main collecting branch from nipple base: 2–6 mm
Distance of first branch of main duct from nipple base: 3–13 mm
Depth of first branch: 5–11 mm
60%–80% of glandular tissue is within a 30 mm radius of base of nipple
Ducts (Refs. 30, 34, and 37)
Number of main ducts: 14
Ducts opening at nipple: 4
Main duct diameter: 3 mm
Mean diameter of main ducts at base of nipple: 1–4 mm
Number of main ducts between 4 and 18 but not all open at nipple
Diameter of ducts converging at nipple: 2–4.5 mm (Ref. 31)
Fat (Refs. 30, 34, and 37)
Fat content: subcutaneous fat: 17%–31%, intraglandular fat: 2%–12%, retromammary fat: 4%–10%
50% of the intraglandular fat is present within the 30 mm radius of the base of the nipple
Areola and nipple (Refs. 30, 34, and 37)
Mean areola radius: 20–32 mm
Nipple diameter: 13–17 mm
Ribs (Ref. 39)
Ribs average cross-sectional height: 9–16 mm
Ribs average cross-sectional width: 6–12 mm
Muscle (Ref. 38)
Muscle average total width: 200 mm
Muscle average total length: 150 mm
Muscle approximate thickness: 15 mm
Tissue proportions (Ref. 31)
55% fat (10% retromammary; 7% intraglandular; 38% subcutaneous)
45% gland

within—similar to observations on an MRI or Ultrasound image. Ductal diameters, distribution, and branching closely mimic anatomy^{30,37} and ultrasound measurements.^{34,35}

In this paper, we report two 3D breast designs with different levels of detail. In the first level phantom, we model a simple 3D structure of the breast with all the layers homogeneous—as a lumped model. We still retain the contours and

shape of the breast. Such a model is obviously not realistic but offers a rapid way to test simulations. The main drawback is that the glandular structure is lumped and not diffuse. The second level software phantom (see Sec. III C) replaces the lumped glandular region with a ductal tree structure realizing only the primary ducts, lobes, and lobules. Alveoli within the lobules, smaller ductal branches, Cooper's ligaments, and fat are not explicitly modeled. They stay the same as in the first level description. In this level, the amount of fat and glandular tissue can be varied easily (for example, by adding additional ductal branches), that quite often varies with age, pregnancy, lactation, menstrual cycle, and menopause.

III.B. Measurements and specifications

Images of breast anatomy from the literature^{30,31,34,37–39} were used as a visual guidance to develop the models involved in this study. The exact figures used are omitted from this paper due to permission costs. Surveying these books, breast structure specifications and dimensions were established and summarized in Table I.

III.C. Creation

In this section, we outline the way in which the design tool (SOLIDWORKS) was used to create the breast phantom. Figure 1 shows a highlight of the process and in detail creation of the difficult elements—ductal branches, lobules, and tumor. The details are covered in Appendix A. The first step is the creation of breast muscle and ribs [Fig. 1(a)]. First, the *pectoralis muscle* was created. This is the bed of the breast. It provides a frame of reference for the other layers created above it. Here, approximately two-thirds of the bed is comprised of *pectoralis major muscle* and the rest is *serratus anterior muscle*. The diameter of the bed base is 144 mm and the approximate thickness of the muscle is 11 mm. Next, we created five rib-sections (depicting second through sixth pair of ribs) that lie right below the breast in the form of a circular cut-out from the chest. The distance between the centers of ribs was set as

Design of the 3D software phantom: Overall illustration

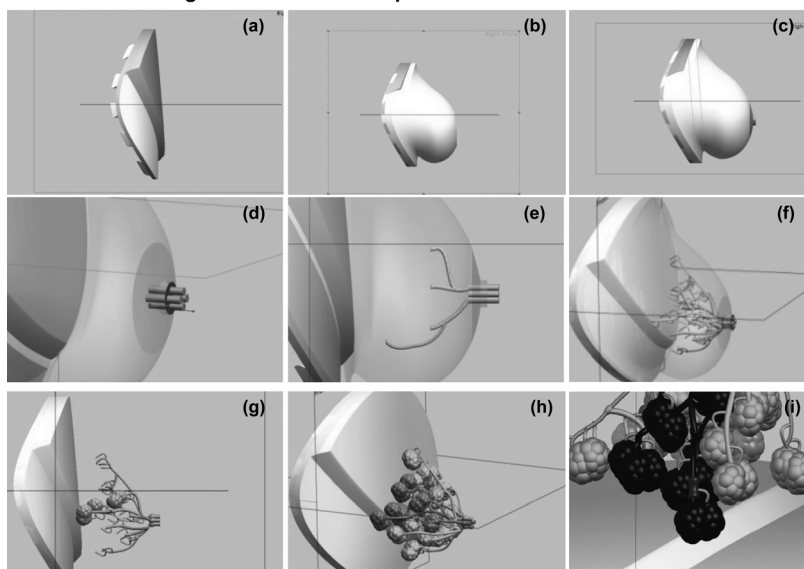


FIG. 1. Creation of (a) Ribs and muscles; (b) breast boundary; (c) nipple; (d) establishing four main ducts; (e) 1 set of ducts; (f) ductal tree structure; (g) lobes; (h) all 10–20 lobes; and (i) tumor in duct. All details of these images are in Appendix I.

14 mm. The height of the rib along the coronal plane of the breast was 14 mm. The width of the rib along the transverse plane was approximately 6 mm and the thickness of the intercostals muscles was approximately 6 mm. Next, we built the *serratus anterior muscle layer*. The thickness of *serratus anterior muscle* was set approximately to 4 mm. Again, the details are omitted but creation follows ideas presented in Appendix A.

Next, we built the breast contour [see Fig. 1(b)]. The height, width, and depth of the breast were set approximately to 144, 144, and 72 mm, respectively. The diameters of the areola and nipple were set to 40 and 12 mm, respectively [Fig. 1(c)]. Appendix A presents the idea behind creating this boundary. Next, we created the ductal tree depicting the branches present in the glandular region. We created four milk ducts that converge at the nipple [see Fig. 1(d)], each of which has a lactiferous sinus bulge. These four ducts branch out into multiple smaller ducts as they run down [Fig. 1(e)]. Each of these smaller ducts further branch into even smaller ducts [Fig. 1(f)] terminating with a lobe [Fig. 1(g)]. The diameter of the branches converging at the nipple was 3 mm. The diameter of the lactiferous sinus bulge was 4 mm and the length was 6 mm. The diameter of the branches in the fat region was 2 mm and the diameter of the branches terminating in the lobule was 1.2 mm. Appendix A describes the method of creating the ductal branches in detail. The last step was the creation of the lobules and the tumor. The glandular area in a female breast primarily resides in the center of the breast and typically contains 10–20 lobes, each comprised of smaller lobules that are clumped together [see Fig. 1(h)]. The diameter of the lobule was 3 mm, the diameter of the lobe was approximately 9 mm and the length was approximately 11 mm. For the purpose of illustration, we have shown here a dumbbell shaped tumor placed in a duct used [see Fig. 1(i)]. The diameter of each dumbbell was 4 mm with the overall length of 7.5 mm. We also use spherical shaped tumors (5 mm diameter) and irregular-shaped tumors. Appendix A describes the method of creating the lobes and the tumor.

IV. BIOMECHANICAL MODELING

Biomechanical modeling using FEM techniques has been explored to predict mechanical deformations on the breast during applications like a biopsy procedure, mammography,² and improving the predictions of elastic modulus in *elastography*⁴⁰ among others. Different biomechanical breast models will vary mainly with respect to the mesh generation, boundary conditions used, and the assumed tissue properties. As the underlying application dictates the magnitude of deformation encountered in the biomechanical breast model, prediction accuracy is also application specific. One drawback of FEM based biomechanical models is that they are generally difficult to implement and have long processing time especially for more complicated geometries. According to Rajagopal *et al.*,² there are three major requirements for developing a realistic biomechanical model of the breast. First, accurate geometric representation of the anatomy of the breast for the given application, second, constitutive models that faithfully represent the mechanical behavior of different tissues and third, realistic and precise representation of

boundary and loading conditions. The fidelity of these aspects determines the accuracy of breast mechanics predictions.

For our application of *elastography*, an FEM biomechanical model was created using COMSOL 4.1 on the second level 3D breast phantom. In subsections IV A–IV C, we describe the experiment and the FEM settings in detail.

IV.A. Elastography: Typical experiment

We simulate a typical *elastography* experiment of applying a static stress to a local surface on the breast phantom just above a simulated tumor so that the tumor experiences maximum stress when compressed. The area of stress application is defined as 60×19 mm to simulate a clinical linear array transducer with a small plate attached to it. This type of stress application is typical of static clinical *elastography*, where, the technician locates the tumor first and then compression is applied on the surface of the breast in a plane to include the tumor. As a result, we did not vary the location of the imposed stress, as the stress location was dependent on tumor location. For the simulations, we applied a force of 4 N. This magnitude of force was chosen from the clinical *elastography* work of Sridhar *et al.*,⁴¹ where the authors applied incremental forces from 0 to 10 N on breasts of volunteers and estimated average glandular strain with a clinical ultrasound scanner. 4 N was suggested the maximum force to engage linear behavior in the breast that caused a finite strain of approximately 5%. We use this force as our input in the simulation and apply linear models. Clinical freehand *elastography* in many instances also involves larger compressions greater than what is reported in this paper. However, the authors wanted to demonstrate the first step of linear modeling to test this software breast phantom in the context of *elastography*. We are also currently pursuing nonlinear modeling efforts to model larger deformations with hyperelastic properties but optimizing the solver configurations is nontrivial for these complicated geometries and will not be covered in this work.

There are several parameters that can be modified in this phantom: (a) parameters that are inherent to the breast geometry (modified through SOLIDWORKS); (b) material properties (modified through the FEM framework of COMSOL), and (c) extent and location of applied force (4 N in this case for linear modeling⁴¹ with location on the surface of the breast just above the tumor).

In this paper, the main objective was a FEM parametric study of *elastography*, where the parameters investigated are location of the tumor at different depths, stiffness of the tumors, shape of the tumor, and analysis in 2D vs 3D. These parameters have been shown to be important in clinical *elastography*. For instance, decreased contrast has been documented for deep tumors;²⁶ difficulties have been noted in differentiating all types of benign (spherical, low stiffness tumors) and malignant (irregular, high stiffness tumors) (Refs. 27 and 28); and errors have been noted during modulus reconstruction when 2D displacement or strain information was used.¹⁷ In particular, we investigated strain contrast and CTE changes between tumors of different shapes (spherical, dumbbell, and irregular) placed deep and shallow within glandular tissue for two levels of stiffness contrast (6 dB and 20 dB) between the tumor and

background. We do this in 3D with no approximations and in 2D with a plane strain approximation. We also compare results with a commonly used *elastography* phantom (simple rectangular phantom with spherical inclusion). Currently, we do not use this framework to test an inverse problem.

The CTE in decibel is defined as the difference between the absolute value of the measured strain contrast in decibel and the absolute value of the modulus contrast in decibel.¹⁸ The modulus contrast was defined as the ratio of the modulus of the inclusion to the modulus of the background. The strain contrast was defined as the ratio of the strain in the background to the strain in the inclusion.

To achieve 6 dB or 20 dB input tumor-background modulus contrast, the background region-of-interest (ROI) is first chosen as a circle (in 2D) or a sphere (in 3D) around the circular (in 2D) or spherical (in 3D) tumor. The background ROI is at least 4–8 times the area (in 2D) or volume (in 3D) of the tumor. To compute CTE across the parameters of interest, the ROI is selected such that the mean value is constant across all cases (deep, shallow, 6 dB, 20 dB, and tumor shapes). To achieve this, the radius of the background ROI circle or sphere was modified slightly. The tumor is then assigned double the value (for 6 dB contrast) and 10 times the value (for 20 dB contrast) of the background. The background value of the block phantom is then assigned this value. Once the simulations are setup, they are made to run until a convergent, mesh optimized solution (see Sec. IV C) has been achieved. When comparing to the block phantom, we ensure that the mean value of the selected ROI for the background is equal to the value assigned to the background of the block phantom to allow for a fair comparison. The same areas are used for strain and modulus calculations.

We also show three types of inclusions within the breast phantom—spherical-shaped inclusions, irregular-shaped, and dumbbell-shaped inclusions to illustrate the flexibility of the phantom to tumor shape. Also breast tumors occur in different irregular shapes such as the above. Among these, spherical inclusions that mimic a fibroadenoma (benign tumor) have been shown to display the lowest CTE when compared to other cylindrical inclusions.¹⁸ Irregular and dumbbell shaped tumors have also been seen clinically as reported by Thitaikumar *et al.*⁴²

IV.B. Constitutive equations for FEM

As discussed above, *in vivo elastography* measurements of breast tissue have shown that under small compressions, the tissue behaves linearly.⁴¹ Using these assumptions, it is possible to define breast tissue's Young's modulus E_i as a function of applied strain ϵ_i for a particular tissue type i . Under these conditions, the infinitesimal strain tensor provides a good approximation of the deformation measurement. The stress tensor then depends linearly on the components of strain tensor. If X, Y, Z are the three principal directions and u_X, u_Y, u_Z are the displacement vectors in the corresponding directions, then the infinitesimal strain tensor can be defined as

$$\epsilon_{ij} = \frac{1}{2} \left(\frac{\partial u_i}{\partial j} + \frac{\partial u_j}{\partial i} \right). \quad (1)$$

The strain components when $i = j$ are the normal direct strains and are shear strains when $i \neq j$. If the applied stimulus does not produce a translation or a rotation of the whole body, out of the nine components of stress and strain, only six remain independent. We can assume that under ideal conditions, static *elastography* with an external compressive stress does not cause any rotation or translation. Standard constitutive equations⁴³ govern the relation between stresses (σ_{ij}) and strains (ϵ_{ij}) through material properties like shear modulus (G) and bulk modulus (K) for isotropic media. Breast tissue has commonly been assumed to be isotropic.^{44,45} Furthermore, since the equations are being derived for FEM analysis, where all of the material properties are modeled locally, it can be assumed that local tissue properties are isotropic and homogeneous. The generalized Hooke's law then governs this relation and is given as

$$\sigma_{ij} = \left(K - \frac{2}{3}G \right) \Delta \delta_{ij} + 2G\epsilon_{ij}, \quad (2)$$

$$\sigma_{ij} = 3K\epsilon_{ijh} + 2G\epsilon_{ijd}, \quad (3)$$

where i, j can take values of the principal directions X, Y, Z , δ_{ij} is the Kronecker delta function and Δ is the trace of the strain matrix. The second equation in this group gives an alternative representation of the Hooke's law where, ϵ_{ijh} , is mean or volumetric infinitesimal strain along the diagonal of the strain matrix (volume changes) and ϵ_{ijd} is the deviatoric infinitesimal strain governing shape changes. $\epsilon_{ijh} = (\Delta/3)\delta_{ij}$ and $\epsilon_{ijd} = \epsilon_{ij} - \epsilon_{ijh}$. With a further assumption of incompressibility⁴⁵ ($\mu \sim 0.5$), i.e., shear modulus (G) \ll bulk modulus (K), $(K - 2G/3)\Delta$ in the above equation is replaced by the isotropic hydrostatic pressure— P . The generalized Hooke's law now becomes: $\sigma_{ij} = -P\delta_{ij} + 2G\epsilon_{ij}$.

The stress matrix can also be expressed in terms of its hydrostatic and deviatoric parts as $\sigma_{ij} = \sigma_{ijh} + \sigma_{ijd}$. Hydrostatic stress is the mean of normal stresses (along the diagonal of the stress matrix) and is the state of stress, when all three principal stresses are equal to each other, analogous to the stress in a fluid in a static state. Deviatoric stress is a measure of changes in shape not volume. Again, $\sigma_{ijh} = (\sum/3)\delta_{ij}$, where \sum is the trace of the stress matrix.

From the above equation [Eq. (2)], $\sigma_{ijd} = 2G\epsilon_{ijd}$ and $\sigma_{ijh} = 3K\epsilon_{ijh} = -P\delta_{ij}$. Adding mean and deviatoric parts, separating coefficients, and writing in matrix form gives the stress tensor equation for independent terms as

$$\begin{pmatrix} \sigma_{XX} \\ \sigma_{YY} \\ \sigma_{ZZ} \\ \sigma_{XY} \\ \sigma_{YZ} \\ \sigma_{XZ} \end{pmatrix} = \begin{pmatrix} -P & 0 & 0 & 0 & 0 & 0 \\ 0 & -P & 0 & 0 & 0 & 0 \\ 0 & 0 & -P & 0 & 0 & 0 \\ 0 & 0 & 0 & 0 & 0 & 0 \\ 0 & 0 & 0 & 0 & 0 & 0 \\ 0 & 0 & 0 & 0 & 0 & 0 \end{pmatrix} + G \begin{pmatrix} 4/3 & -2/3 & -2/3 & 0 & 0 & 0 \\ -2/3 & 4/3 & -2/3 & 0 & 0 & 0 \\ -2/3 & -2/3 & 4/3 & 0 & 0 & 0 \\ 0 & 0 & 0 & 2 & 0 & 0 \\ 0 & 0 & 0 & 0 & 2 & 0 \\ 0 & 0 & 0 & 0 & 0 & 2 \end{pmatrix} \begin{pmatrix} \epsilon_{XX} \\ \epsilon_{YY} \\ \epsilon_{ZZ} \\ \epsilon_{XY} \\ \epsilon_{YZ} \\ \epsilon_{XZ} \end{pmatrix}. \quad (4)$$

Similar analysis can be followed if strains are the measured quantities, then for incompressible media, the bulk compliance, $B \rightarrow 0$, and $\epsilon_{ij} = (1/2)J\sigma_{ijd}$ (volumetric part of the strain is zero). Here, J is the shear compliance. Hence, the matrix form is

$$\begin{pmatrix} \epsilon_{XX} \\ \epsilon_{YY} \\ \epsilon_{ZZ} \\ \epsilon_{XY} \\ \epsilon_{YZ} \\ \epsilon_{XZ} \end{pmatrix} = J \begin{pmatrix} 1/3 & -1/6 & -1/6 & 0 & 0 & 0 \\ -1/6 & 1/3 & -1/6 & 0 & 0 & 0 \\ -1/6 & -1/6 & 1/3 & 0 & 0 & 0 \\ 0 & 0 & 0 & 1/2 & 0 & 0 \\ 0 & 0 & 0 & 0 & 1/2 & 0 \\ 0 & 0 & 0 & 0 & 0 & 1/2 \end{pmatrix} \times \begin{pmatrix} \sigma_{XX} \\ \sigma_{YY} \\ \sigma_{ZZ} \\ \sigma_{XY} \\ \sigma_{YZ} \\ \sigma_{XZ} \end{pmatrix} \tag{5}$$

COMSOL 4.1 implements Eqs. (4) and (5) for calculating local stresses and local strains due to applied deformations.

IV.C. Finite element model settings

Solid mechanics FEM package from COMSOL 4.1 was used in this study. The basic FEM setup involves phantom import, meshing, choosing relevant constitutive equations, material models, assigning boundary conditions, and choosing an appropriate solver. Before any forces are applied, we compensate for the gravitational force acting on the model. Since the model was created using illustrations of 3D anatomy in a standing position, it was assumed that gravity was already present. The model was then corrected for gravity for the supine setup—typically the scanning position in *elastography*. Sections IV C (1-4) discuss the various FEM parameters used in this study. The flowchart in Fig. 2 gives the details of the FEM model optimization protocol.

IV.C.1. Material properties

The choice of material properties is critical to the realism of the numerical model. However, we are limited by the data available on *ex vivo* measurements and we make our choices for material properties based on these measurements. Also, other works on breast biomechanical modeling for applications like mammography² have made similar choices but do

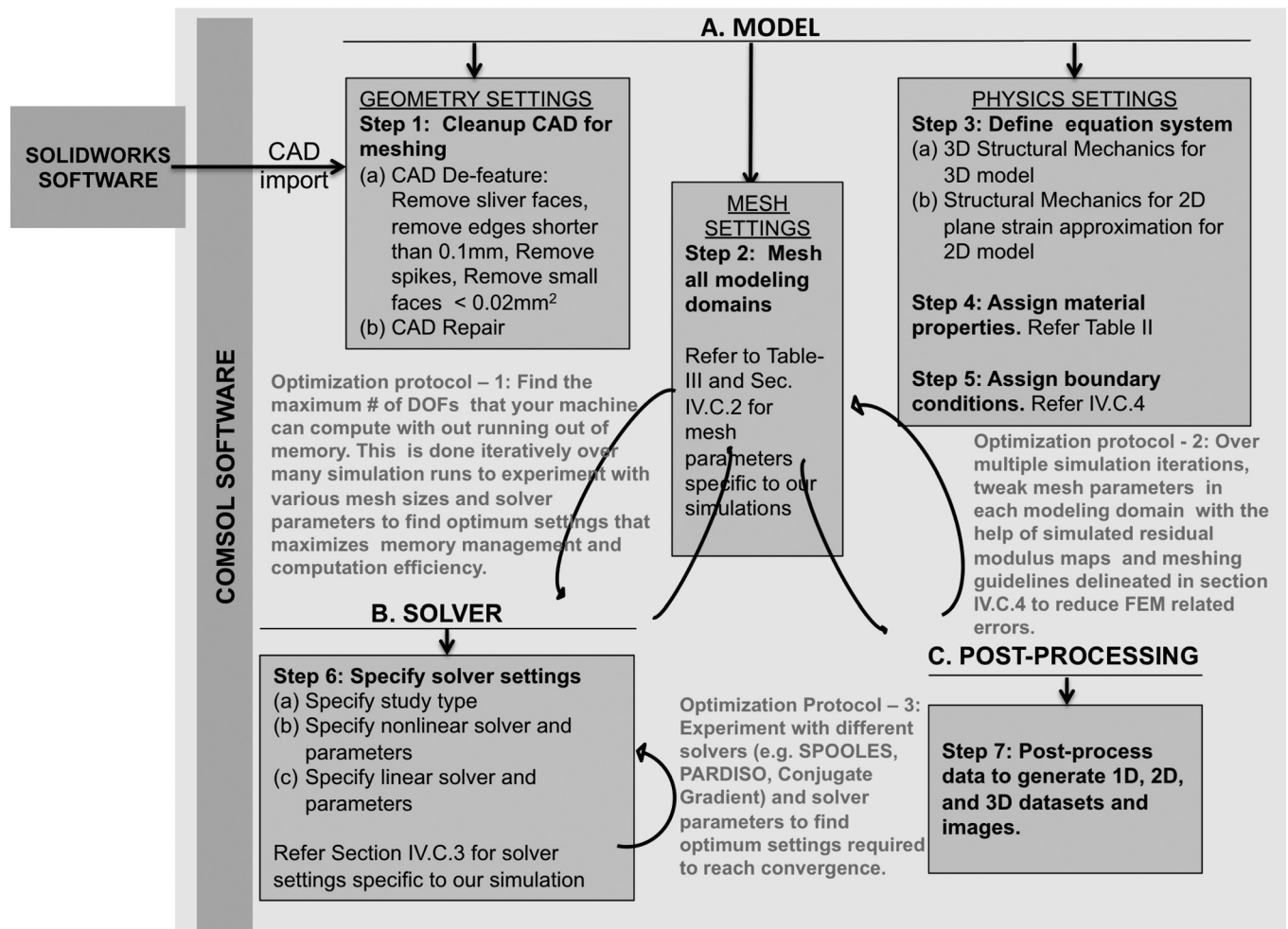


Fig. 2. FEM modeling parameter selection and optimization process.

TABLE II. Material properties.

Properties	Young's modulus: E(KPa)	Poisson's ratio: η
Fat	19	0.49
Gland	33	0.49
DCIS	25	0.49
IDC	93	0.49
Fibroadenoma	107	0.49
Ribs	15 GPa	0.21

point out that the choice of material properties is critical for the validity of the model.

The constitutive material parameters for the above biomechanical model were obtained from the works of Wellman *et al.*,⁴⁵ Azar *et al.*,¹¹ and Krouskop *et al.*⁴⁴ Table II shows the material properties used in our simulations for linear modeling scenarios.

Both Wellman *et al.* and Krouskop *et al.* found approximately a 5% variation in modulus estimates over all types of breast tissue with loading frequencies of 0.1, 1, and 4 Hz indicating that breast tissue behaves more or less in an elastic manner with the viscous components being reduced. We choose 1 s loading time in our simulations.

IV.C.2. Meshing strategies

Typically, in FEM modeling, a variable representing all-over model accuracy is monitored as a way to achieve convergence of the model with minimum errors. To achieve this, the mesh size is increased until that variable becomes mesh independent within reasonable tolerance of error. The variable is generally observed at preselected probe points across the model. In general, such an approach is applicable to simple geometries.

In our model, we could not take an all-over model approach because of the inherent geometric nonlinearity of our breast model. As the breast model requires different density and element size in different regions, regional accuracy needed to be monitored. As a way to track errors, we chose to monitor *residual modulus* as our variable, where *residual modulus* was defined as the difference between assigned elastic modulus and measured axial stress/axial strain ($\sigma_{11}/\epsilon_{11}$). Under an ideal situation of a uniaxial experiment with no internal boundaries, axial stress/axial strain should be equal to elastic modulus. However, this does not happen with the complicated geometry of the breast model, given that all components of stress develop at each voxel. However, these two values are in general very close to each other excepting at the boundaries where the assumptions of a perfect uniaxial experiment are primarily violated.

We tweaked mesh parameters and estimated residual modulus for each simulation run and then over several modifications achieved a mesh independent solution of residual modulus. Finer meshes require more computational power but were not needed for this application. Tracking residual modulus gives us the flexibility to closely monitor and modify mesh size differently in different regions around the model until errors are within reasonable tolerance level.

It is common to use a parameter such as *residual modulus* locally or over the entire geometry. For instance in Rajgopal *et al.*,⁴⁷ eight material points located throughout the model, were used to refine the mesh. Ng *et al.*,⁴⁸ used electric potential at a specific location in the model that was observed for convergence over multiple mesh sizes. Srinivas *et al.*,⁴⁹ determined the best mesh after looking at outputs from five meshes of varying elemental sizes. An acceptable mesh was determined when a further increase in mesh density did not change the output variables. Chen *et al.*,⁵⁰ verified convergence of the solutions by checking strain energy and displacement at four loading points for all the solutions.

We show in Sec. V, 2D and 3D residual modulus maps along with their profiles to illustrate the strategy used for optimizing meshing. Generating residual modulus maps helps to guide us through the meshing process to discretize the modeling domain to appropriately model regions with high geometric nonlinearity and large differences in material properties to reduce simulation errors.

Mesh quality is dependent on various factors that include, but are not limited to, physics being modeled, applied stimulus (stress vs strain), amount of input stress, geometric details, and material properties. Optimizing all these parameters is a nontrivial iterative process. Both 2D and 3D branched models are highly nonlinear in their geometry; therefore, different subdomains had to be meshed separately. We begin with an initial estimate of mesh parameters, run the simulation, visually inspect residual modulus maps and plot 1D profiles. We then tweak mesh parameters in the modeling domain to reduce the simulation errors and boundary effects and then rerun the simulation to repeat the process of inspection and tweaking based on the residual modulus maps. We do this until we reach an upper limit on mesh size and the relative size of mesh elements across boundaries according to the guidelines listed below. At this point if the resulting errors are not acceptable, we experiment with a different solver optimized for the computing power of the machine, or reduce the level of complexity in the modeling domain (2D vs 3D, isotropic material model vs viscoelastic material model, etc.).

IV.C.2.a. Mesh Guidelines

- Upper limit of the mesh size is typically constrained by maximum number of degrees of freedom (DOF) that your machine can compute. This is dependent on the mesh size and the physics being modeled. Going above the upper limit will result in simulation out-of-memory errors.
- Lower limit of the mesh size is typically constrained by the geometric details in the model and the level of deformation experienced in the respective domain.
- Element size should be smaller than the deformation experienced in that region for accurate strain prediction.
- To reduce boundary effects, boundaries that separate domains with a stiffness value jump are meshed slightly coarser than the domains on either side.
- Edge mesh is explicitly defined for boundaries that require a different curvature resolution overriding the default mesh curvature resolution parameter for that domain.

- In general, regions experiencing high stress/strain (like load and fixed boundaries) are meshed finer than the rest of the domains.
- Our optimal mesh settings for the 2D and 3D breast phantom models are listed in Table III and our meshing sequence for all the domains are described below.

IV.C.2.b. Meshing Sequence in 2D. (1) Mesh tumor domain: 0.7–1 mm; (2) mesh glandular domain: 0.2–3 mm; (3) mesh edges along fat domain: 0.7–0.9 mm; (4) mesh fat domain: 1–3 mm; (5) mesh muscle domain: 1–2 mm; and (6) mesh ribs domain: 0.5–1 mm

IV.C.2.c. Meshing sequence in 3D. (1) Mesh edges in rib domains: 1–2 mm; (2) mesh edges in muscle domain: 1–2 mm; (3) mesh edges along breast contour: 2–3 mm; (4) mesh edges along tumor and duct opening on nipple: 1–1.5 mm; (5) mesh tumor domain: 0.5–0.8 mm; (6) mesh ribs and muscle domains: 2–3 mm; (7) mesh left glandular branch: 0.2–2 mm; (8) mesh lower glandular branch: 0.2–1.5 mm; (9) mesh right glandular branch: 0.2–1.5 mm; (10) mesh top glandular branch: 0.2–2 mm; and (11) mesh fat domain: 2–2.5 mm.

IV.C.3. Solver settings

A nonlinear solver, which is an affine invariant of damped Newton method, was used to compute a steady state problem and solve for the tissue displacement fields for both 2D and 3D simulations. A linearized model was formed in each Newton iteration and solved together with a stationary solver; MUMPS for 2D and conjugate gradients for 3D. The residual vector was estimated and the correction was applied to the next Newton iteration. The iterations continued until the relative tolerance of 10^{-4} exceeded the relative error.

For the 2D simulations, a direct linear solver MUMPS (multifrontal massively parallel sparse direct solver) was used. The solver uses LU factorization on the stiffness matrix to compute tissue displacement. The memory allocation factor was 1.2; row-preordering was used with a pivoting factor of 0.1. For the 3D simulations, an iterative algorithm conjugate gradients with left preconditioning was used. Due to the geometric nonlinearity of the breast model, direct linear solvers like PARDISO, SPOLES, or MUMPS failed to converge. A preconditioner: geometric multigrid with V-cycle, a presmoothen: blocked versions of SOR (successive over-relaxation) and a postsmoothen: blocked versions of SORU (SOR with upper

triangle of the matrix) were used. 26 number of iterations were required to reach the tolerance of 10^{-4} .

IV.C.4. Boundary conditions

Assignment of boundary conditions is a fairly straightforward process for all models presented in this study. The boundary conditions were as follows:

1. Dirichlet boundary condition is specified at the chest wall, by constraining displacement to zero in all directions, $w = 0$ on chest wall boundary.
2. Generalized flux boundary condition is specified at the top boundary, which has a boundary load specified as force per unit area, which is $F_A = \text{Force}/\text{Area}$. $\delta = F_A$, where n is the outward unit normal vector on the boundary.
3. Free boundary condition is assigned to the rest of the boundaries. This means that there is no load and no constraint defined on these boundaries, and these are free to deform. These boundaries are bounded by the geometric and physics-induced constraints.
4. For 2D modeling, we solve for plane strain, which assumes that all out-of-plane strain components of the total strain are zero.

Once the above breast phantom is established, modifications are fairly simple. The anatomy/geometry of the breast needs to be modified in SOLIDWORKS and the biomechanics associated with *elastography* has to be modified in COMSOL. A student/researcher who has worked with SOLIDWORKS/AUTOCAD or who is willing to learn these tools, can change the breast contour, add/delete glandular branches, add tumors or different sizes/shapes, or can vary the dimensions of the breast fairly easily. Once these are done, import into COMSOL will allow for changes in mechanical properties, loading conditions, linear/nonlinear modeling scenarios, and elastic/viscoelastic modeling. In fact, the biomechanical model can be combined with other physics simulations like heat transfer to study other therapies like hyperthermia.

V. RESULTS AND DISCUSSION

Figure 3 shows our 3D phantoms created (first and second levels) using the SOLIDWORKS design tool in three views—bottom, side, and top. The first level model shows a lumped view of all breast structures. This is especially useful for quick testing (within minutes) and evaluation of the

TABLE III. Meshing parameters.

Parameter	2D Breast model	3D Breast model
Curvature of resolution	0.4	0.4
Element growth rate	1–1.5	1.5–2
Element size (mm)	0.2–4	0.2–4
Element shape	Free quadrilateral	Free tetrahedral
Average element quality	0.94	0.79
Min. element quality	0.19	0.012
Total elements	Triangular: 300; Quadrilateral: 81,800	Triangular: 115,000; Tetrahedral: 1,163,500
DOF	79,900	4,926,100

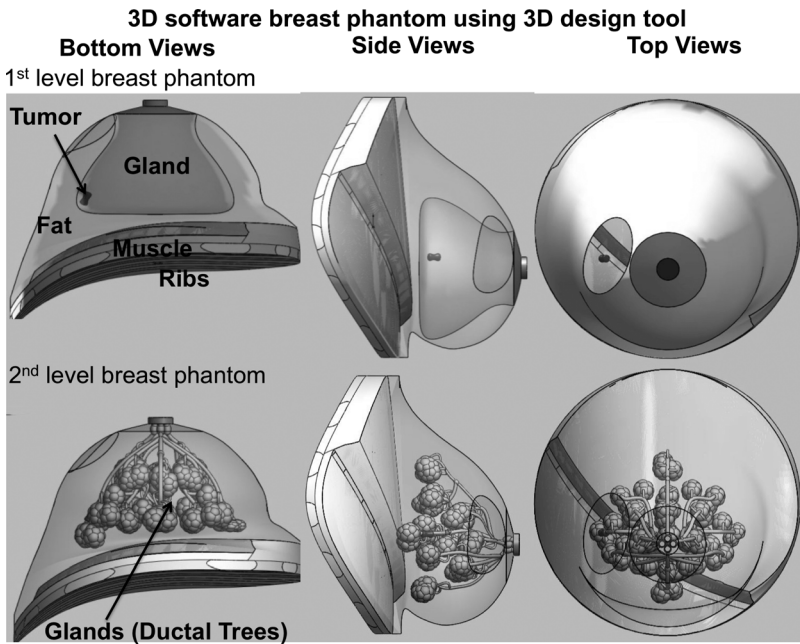


FIG. 3. Our software breast phantom (level 1: lumped and level 2: ductal structures) in three views.

biomechanical model. The second level model shows a detailed ductal branching structure to mimic the breast more realistically. In Fig. 4, we show examples of some of the basic variations that can be done in the 3D design model very quickly for scenarios that commonly occur in the breast with or without cancer. This figure shows the level of flexibility the 3D design tool brings to breast modeling. We show five cases—(a) spherical tumor located deep within glandular tissue within a lobule (to model shape and position change for a tumor); (b) a large 1 cm spherical tumor in a shallow location, just below the nipple (to model size and position change); (c) increase in the ratio of glandular content over fat in the breast (to model scenarios like pregnancy, lactation); (d) change in overall shape of the breast (to model effects of increasing age); and (e) increase in number of lobules in a lobe (to model level of detail achievable in a

lobule) with a dumbbell shaped tumor. These different designs can help in testing or evaluating *elastography* or other imaging technologies in the laboratory after the use of simple physical or software phantoms like block rectangular or hemispherical phantoms before clinical testing.

Shown in Fig. 5 are examples of voxelized and mathematical phantoms from other sources reproduced here with permission to demonstrate other work done in breast phantom design. It is clear that no software phantom can really mimic the breast exactly but can have features represented in them that help in modeling the breast for different applications. While visually comparing our second level model (3) to the other models shown in Fig. 5, our detail is in-between voxelized and mathematical phantoms. We have chosen to model the ductal structures (using the design tool) like mathematical models reported in Bliznakova *et al.*⁷ but have left the fat

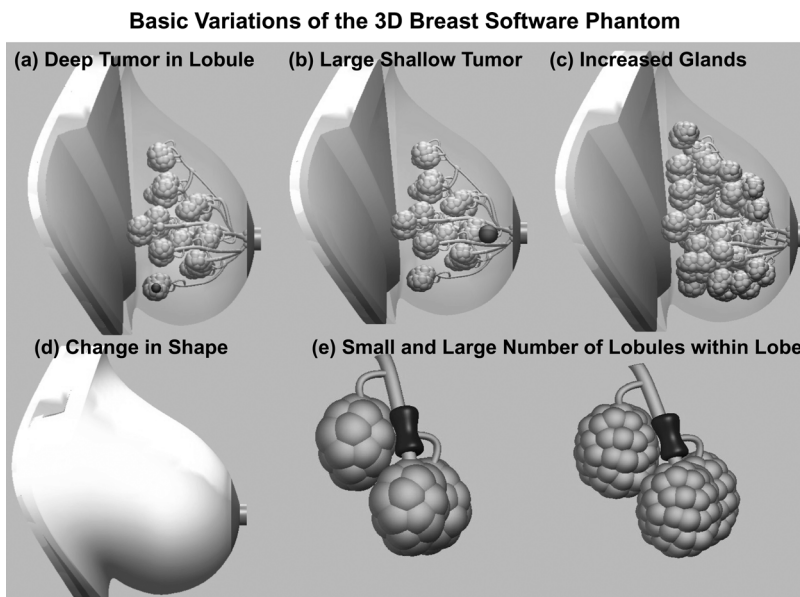


FIG. 4. Illustration of 3D breast phantom with (a) deep spherical tumor located within a lobule; (b) a large 1 cm spherical tumor in a shallow location, just below the nipple; (c) increase in gland to fat ratio; (d) change in overall shape of the breast; and (e) increase in number of lobules in a lobe with dumbbell shaped tumor.

(a) 3D Software Mathematic Phantom (b) 3D Software Voxelized Phantom

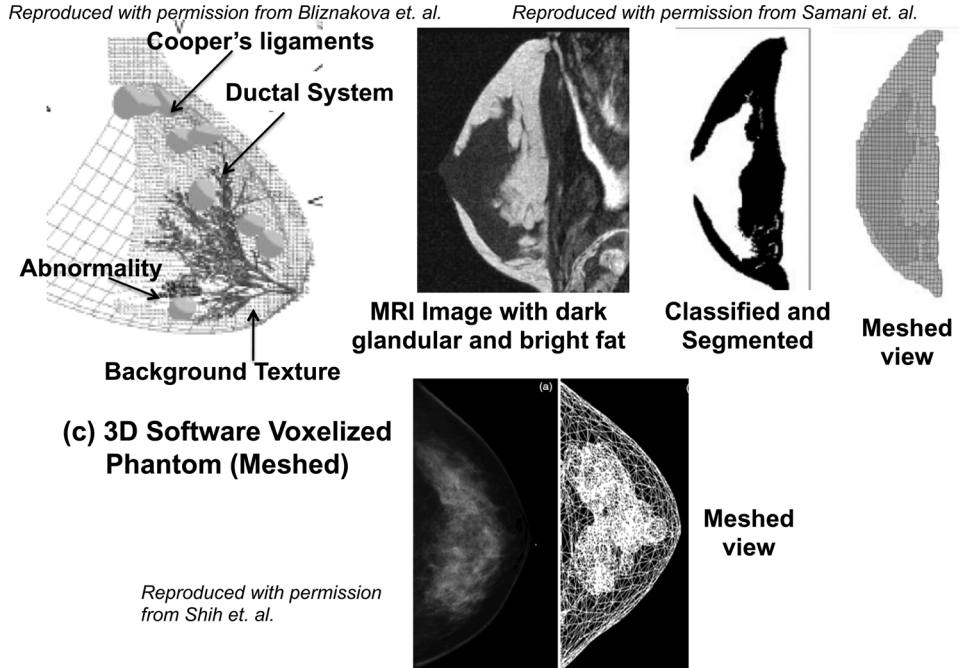


FIG. 5. (a) Example of a 3D mathematical phantom from Bliznakova *et al.* (Ref. 7); (b) example of a 3D voxelized phantom from Samani *et al.* (Ref. 8); and (c) example of a meshed biomechanical model from Shih *et al.* (Ref. 46). Reprinted with permission from, Fig 5(a), Bliznakova *et al.*, A three-dimensional breast software phantom for mammography simulation, *Physics in Medicine and Biology*, **48**, pp. 3699–3719 (2003). Copyright © American Institute of Physics. Reprinted by permission of American Institute of Physics; Fig 5(b), Samani *et al.*, Biomechanical 3-D finite element modeling of the human breast using MRI data, *IEEE Transactions on Medical Imaging*, **20**(4), pp. 271–279. Copyright © IEEE. Reprinted by permission of IEEE; Fig 5(c), Shih *et al.*, Computational simulation of breast compression based on segmented breast and fibroglandular tissues on magnetic resonance images, *Physics in Medicine and Biology*, **55**, pp. 4153–4168 (2010). Copyright © American Institute of Physics. Reprinted by permission of American Institute of Physics.

compartment lumped, like what was reported in Azar *et al.*¹¹ Furthermore, even voxelized models, like what was reported by Samani *et al.* show a lumped fatty region in the breast (see Fig. 5).

We next used our 3D breast phantom with ductal branches (second level) to illustrate the basics of *elastography* using biomechanical FEM modeling in 3D (with no approximations) and in 2D (with a plane strain approximation). To achieve these, the first step was conversion of the 3D design model into a biomechanical model by phantom import and meshing. Figure 6 shows the conversion of the

3D phantom into a meshed biomechanical model using COMSOL 4.1, where, Sec. IV C describes the parameters used in this process. While comparing other examples of meshed software voxelized phantoms from Samani *et al.*⁸ and Shih *et al.*⁴⁶ [see Figs. 5(b) and 5(c)], our meshing strategy visually looks similar (see Fig. 6).

To achieve optimal meshing conditions, we used residual modulus, as a way to guide our meshing strategy. Residual modulus is defined as input modulus—estimated modulus, where estimated modulus is defined as $\sigma_{11}/\epsilon_{11}$. Section IV C and the flowchart in Fig. 2 give all the details of this

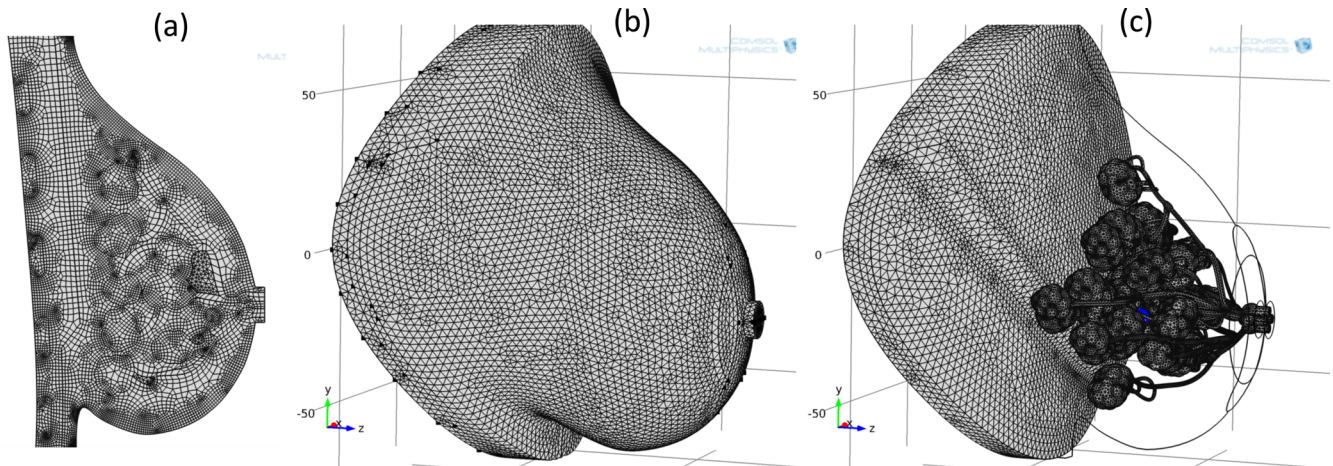


FIG. 6. (a) 2D meshed view, (b) overall 3D meshed view, and (c) meshing of the glandular region. Parameters for meshing are detailed in Sec. IV C.

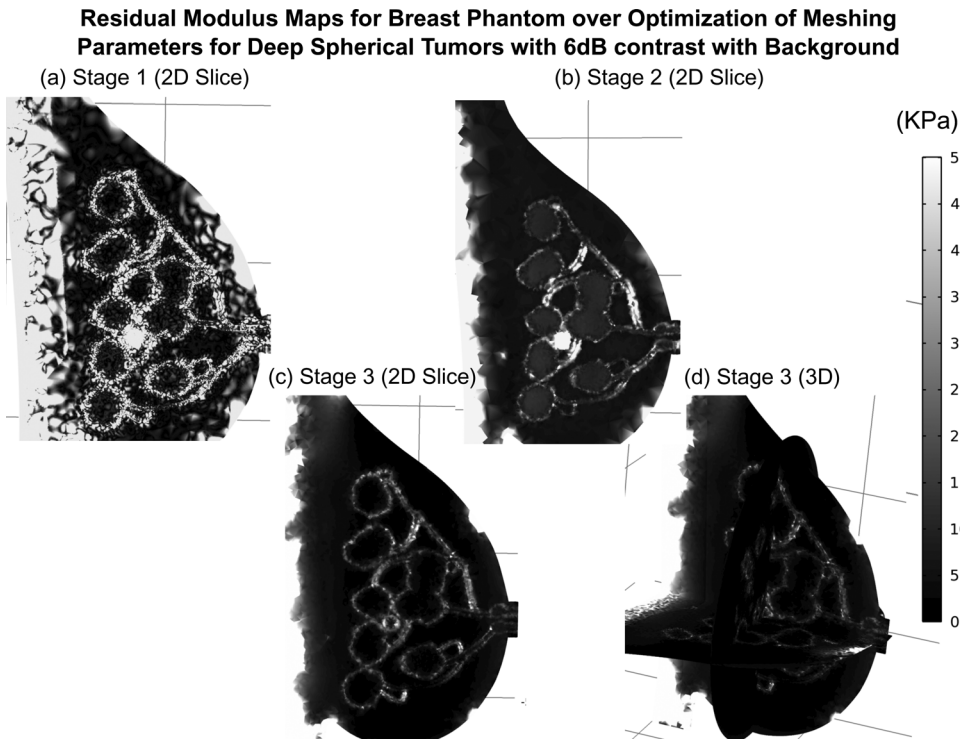


FIG. 7. 2D slices and 3D maps of residual modulus reflecting the 3D mesh optimization procedure. (a) Shows stage 1 of the procedure with initial guesses of the mesh parameters; (b) shows stage 2 with some tweaking; (c) shows stage 3 with final optimized parameters after several iterations of stage 2; and (d) 3D view of residual modulus maps after mesh parameter optimization.

optimization procedure. We show in Figs. 7(a)–7(d), 2D slices of the 3D residual modulus maps generated during this meshing optimization. Stage 1 [Fig. 7(a)] shows large errors at all boundaries and within the tumor. This map was generated with an initial guess of mesh parameters and subsequent discretization of the domain. In stage 2 [Fig. 7(b)], the mesh parameters have been tweaked to reduce the residual modulus significantly. This was done, for example, by reducing the element size at the breast boundary close to the area of stress application and increasing the element size in the tumor region. Stage 3 [Fig. 7(c)] shows the best possible residual modulus map after several iterations of stage 2, i.e., trial and error of modifying the element sizes all around the breast geometry. Stage 3-3D [Fig. 7(d)] shows the residual modulus in all three dimensions of this meshing optimization procedure to demonstrate decreased errors in all 3 dimensions. From Figs. 7(c) and 7(d), it is clear that the residual modulus has significantly improved from stage 1 but is non-zero. There are two main reasons for that—(1) input modulus and estimated modulus (using normal axial stress and strains) are close in value but can never be equal, given, all stress and strain components develop in this breast model; (2) limitations of the computational power of the machine running COMSOL, i.e., there is an ultimate limit on the overall number of elements that the machine can handle. In our case, we have used an Intel core 2.8 GHz with 16 GB of RAM for this task and the maximum number of elements it handles is 5×10^6 . However, these residual modulus maps have proved to be an excellent way to optimize meshing conditions for this complicated geometry.

Figure 8 shows 1D profiles of the residual modulus maps from Fig. 7 expanded for both the breast and branch phantoms for deep and shallow tumors with 6 dB tumor-background contrast. We show absolute errors and relative percentages as well. We see from Fig. 8 that error in the breast phantom is primarily localized at tumor and lobular boundaries (see Fig. 7 for all the cases we explore in this paper.) These residues are related to the extent of geometric nonlinearities in the model and increase when meshing regions with a large difference in material properties. This set of optimized meshing parameters is used in the paper.

Once meshing was achieved, boundary conditions, solver configurations, material models, and input stress/strain stimuli were defined (Sec. IV C). In particular, for this paper, we applied a 4 N force on the surface of the breast just above the tumor. Figure 9 shows the load boundary with reference to the breast areola and nipple. The shape of the load boundary was chosen to mimic a linear array transducer commonly used in *elastography* in the clinic. The figure also shows the extent of displacement (around 5 mm) after the load of 4 N was applied. This level of deformation was achieved when an input modulus distribution shown in Fig. 10(a) was used. The exact values of modulus are shown in Table II.

The figure [Figs. 10(a) and 10(b)] also shows the pre-boundary and postboundary contours and displacement under this force. Again, we see the maximum displacement around 5 mm [Fig. 10(b)] near the load boundary (see the arrows in the Fig. 10(a) for applied deformation.) Similar images for modulus distribution and displacement are shown for a rectangular block phantom with spherical inclusion in

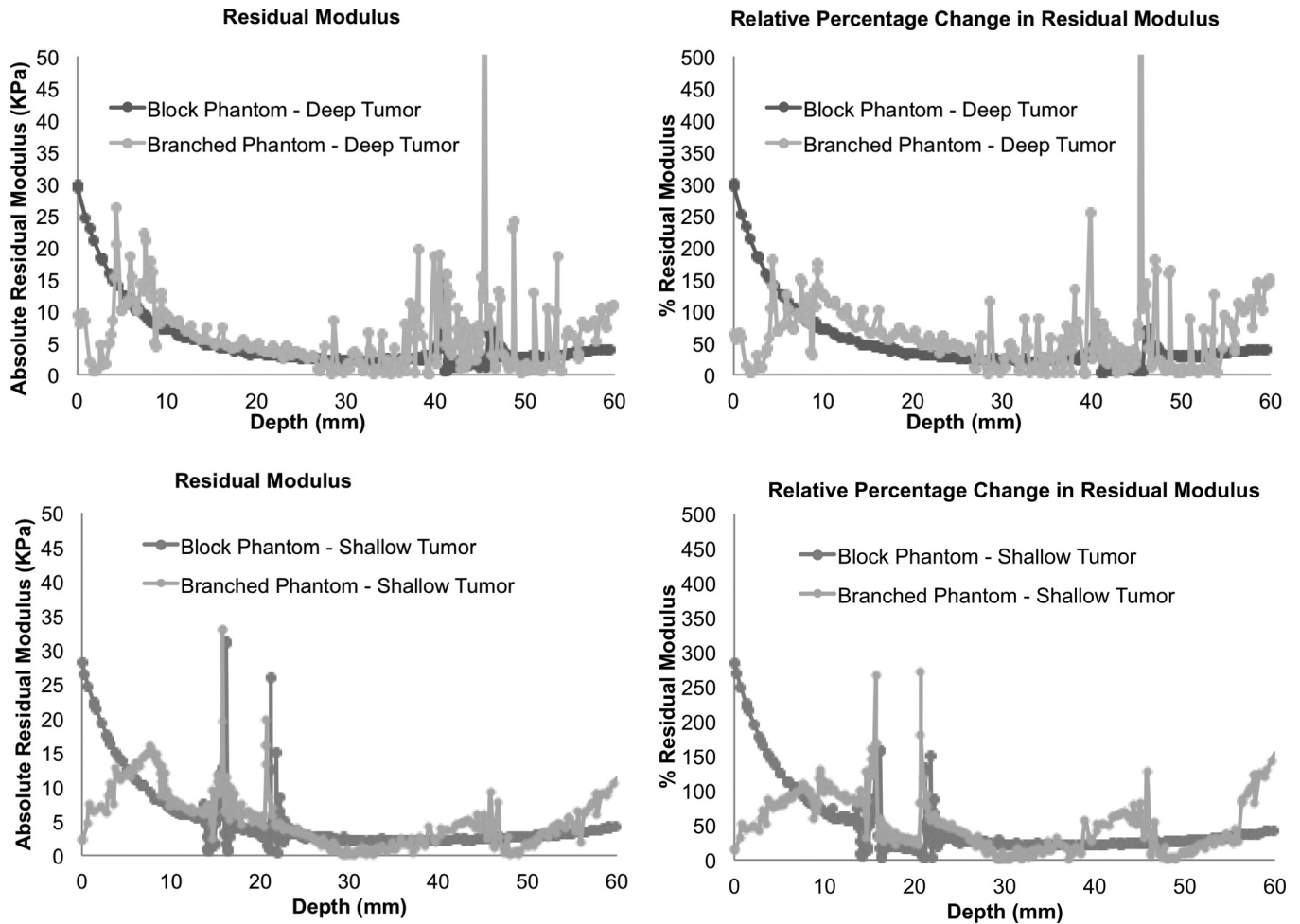


Fig. 8. Profiles of residual modulus with depth for tumors. (a) shows absolute residual modulus for 6 dB input tumor-background modulus contrast for a deep tumor, (b) shows relative percentage residual modulus for 6 dB input tumor-background modulus contrast for a deep tumor, (c) shows absolute residual modulus for 6 dB input tumor-background modulus contrast for a shallow tumor, and (d) shows relative percentage residual modulus for 6 dB input tumor-background modulus contrast for a shallow tumor.

Input Load Boundary and Displacement (Top View)

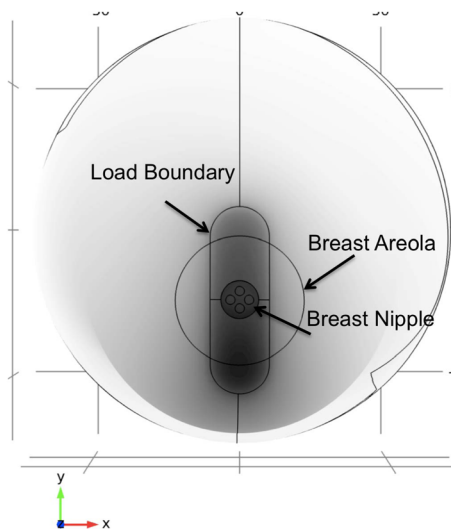


Fig. 9. Top view of the 3D displacement image of the branched breast phantom demonstrating the loading boundary. The figure also shows the extent of displacement, in the colorbar, achieved with the 4 N force applied to the loading boundary.

Fig. 11. This simple phantom is commonly used in *elastography* simulation in the literature and is compared against our branched breast phantom. The load boundary on this phantom is indicated on Fig. 11(a) by arrows.

We show below 2D [see Fig. (12)] and 3D (see Fig. 13) normal axial strain images for the applied 4 N deformation on the top surface of the breast just above the tumor. From the figures, we compute CTE to look for differences between 2D and 3D and breast and block phantoms. 2D results were obtained under plane strain approximations. Figure 12 also shows the corresponding results for the block phantom for 6 and 20 dB input tumor-background modulus contrast at shallow and deep locations of the tumor. All of the strain images have been scaled exactly in values and aspect ratio and their gray-scale contrast is represented by the single adjacent colorbar.

We see strains around 3%–6% in tumor and background regions for a 4 N force. In fact, Sridhar *et al.*,⁴¹ showed approximately 5% strain in glandular regions of normal breast tissue for a 4 N surface applied force. We see a similar range of strain within the lobules. From these figures, tumor

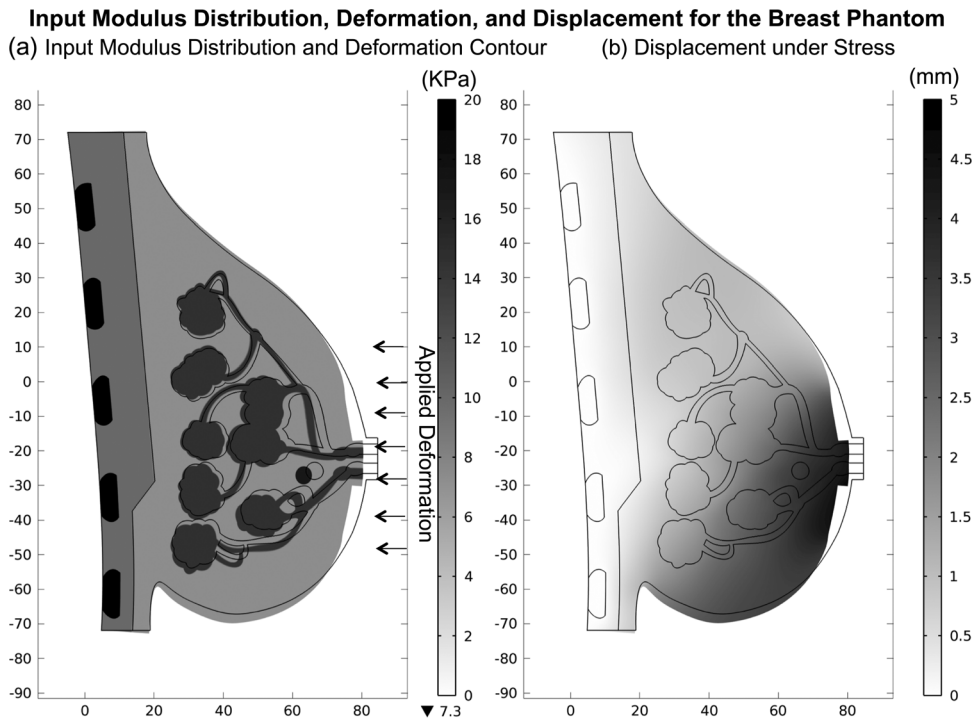


FIG. 10. (a) Input modulus distribution in the branched breast phantom (2D slice) according to Table II. Also shown is the deformation contour after a 4 N force is applied on the top surface of the breast (see arrows) and (b) 2D displacement image due to a 4 N force applied on the top surface of the breast just above the nipple.

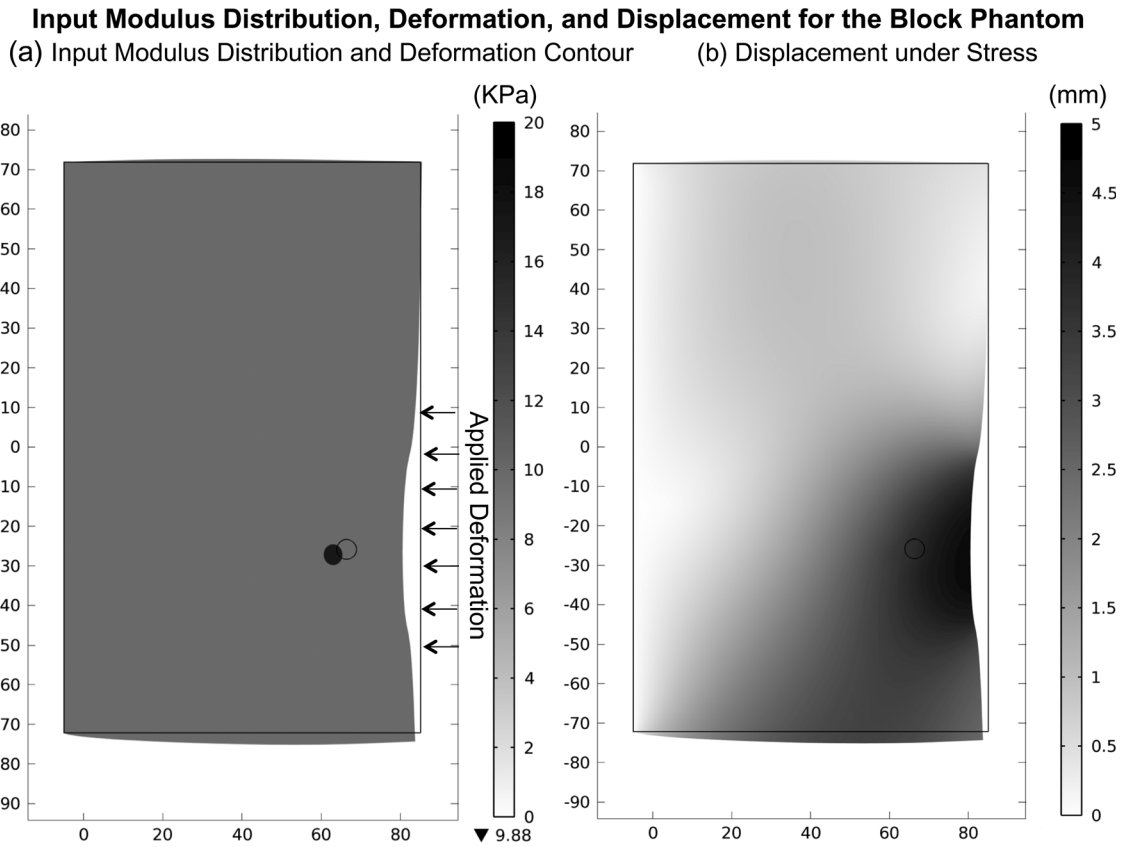


FIG. 11. (a) Input modulus distribution in the simple block phantom (2D slice). Also shown is the deformation contour after a 4 N force is applied on the top surface of the block (see arrows) and (b) 2D displacement image due to a 4 N force applied.

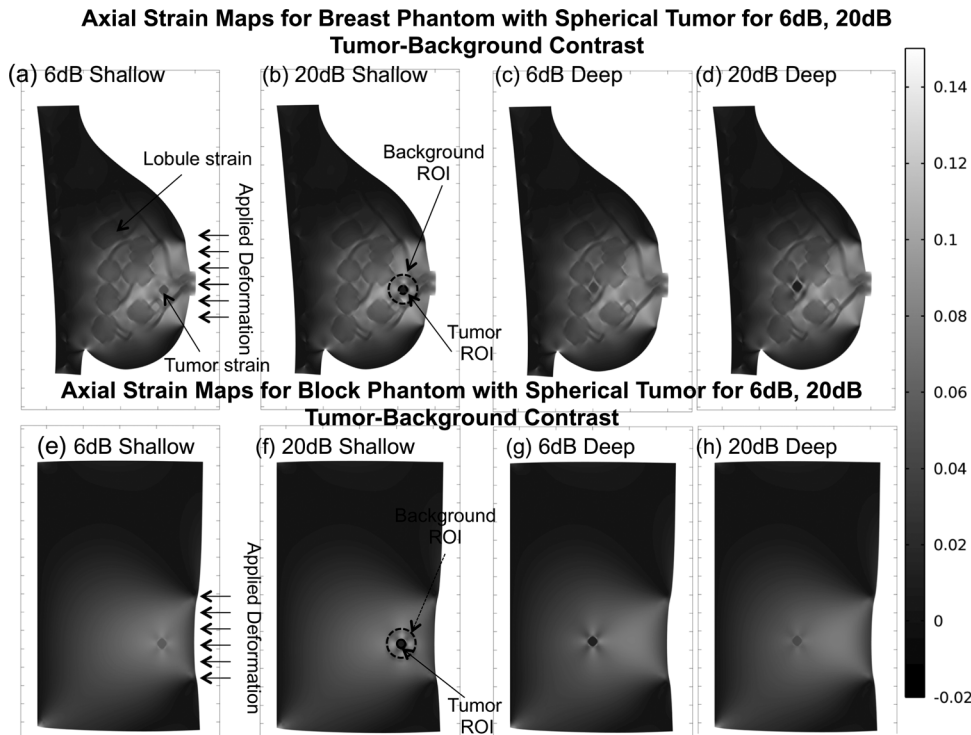


FIG. 12. (a)–(d) 2D Normal axial strain images of the breast phantom for shallow and deep tumors with 6 or 20 dB input tumor-background contrasts. Also shown is the location of the applied deformation and the specific ROI over which CTE analysis was performed for shallow tumors. (e)–(h) Corresponding images for the block phantom. For all the phantoms a 4 N force was applied.

strain intensifies with increase in stiffness contrast (from 6 to 20 dB) for both block and branched phantoms as expected. There seems a small difference in strain contrast observed in the breast phantom for shallow and deep locations. This difference is indistinguishable in the block phantom. However, ROI analysis below with CTE will give finer details.

Figure 12 shows an example background and tumor ROI used to compute CTE. The ROI varies slightly in its radius for deep and shallow locations to ensure that the background modulus value is the same across all the investigated parameters. The block phantom background value then gets assigned this value for a fair comparison.

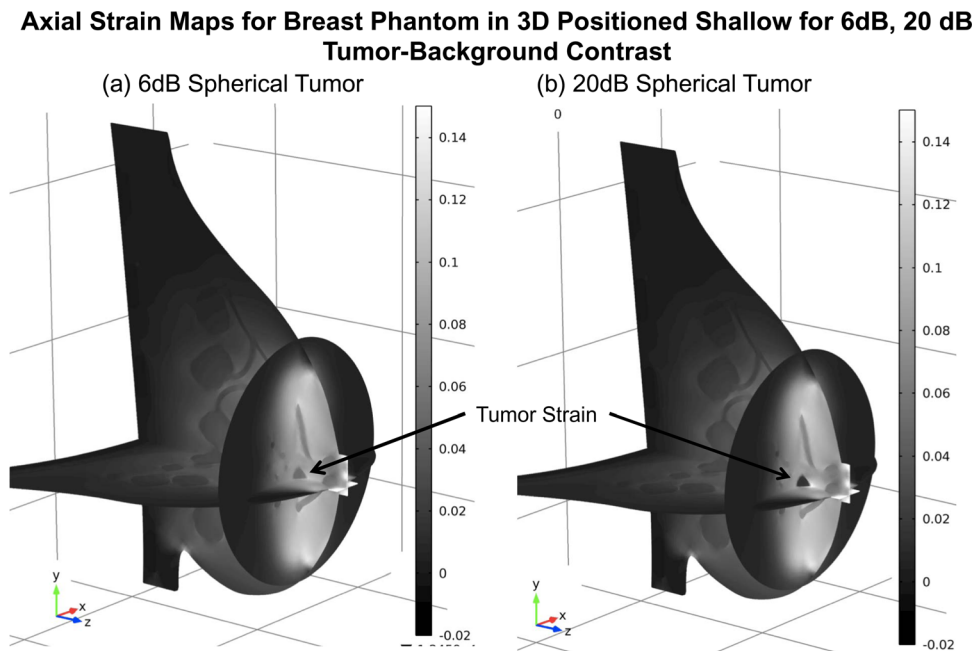


FIG. 13. (a) 3D Normal axial strain images of the breast phantom for shallow 6 dB spherical tumor. (b) 3D Normal axial strain images of the breast phantom for shallow 20 dB spherical tumor.

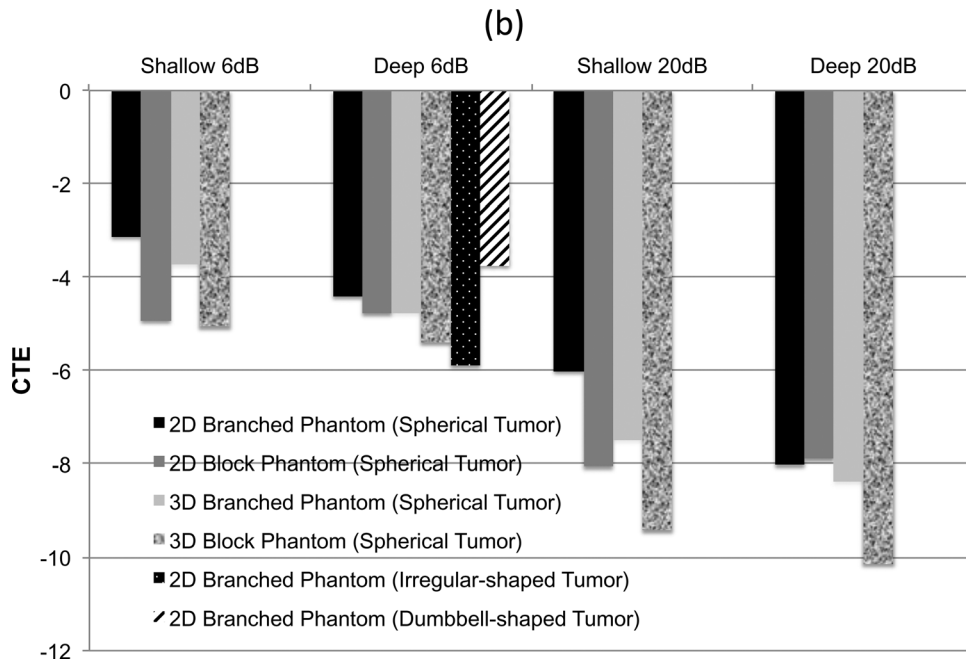


FIG. 14. CTE in dB

Next, we calculated CTE (Fig. 14) and % decrease in contrast by mapping strain (Fig. 15) by calculating average strain and modulus over the ROI for all 2D and 3D breast and block phantom images for the two tumor-background modulus contrasts (6 dB, 20 dB), two depths (deep and shallow), and the three tumor shapes (spherical, dumbbell, irregular). From these figures, the following observations can be drawn—(a) the branched phantom in both the 3D and 2D simulations displayed a superior CTE and a lower loss of contrast (modulus to strain) over the block phantom; more prominent for tumors located in shallow

regions; (b) the breast phantom showed differences in the CTE for shallow and deep tumors with a worse CTE for tumors in deep locations in both 2D and 3D simulations. Little difference was seen in the block phantom for tumors at different depths; (c) 3D simulations with no approximations showed worse CTE values than the 2D counterparts; (d) increase in stiffness contrast from 6 dB to 20 dB worsened the CTE in 2D and 3D for both block and branched phantoms; and (e) the irregular tumor showed the worst CTE values when compared to the spherical and the dumbbell shaped tumors.

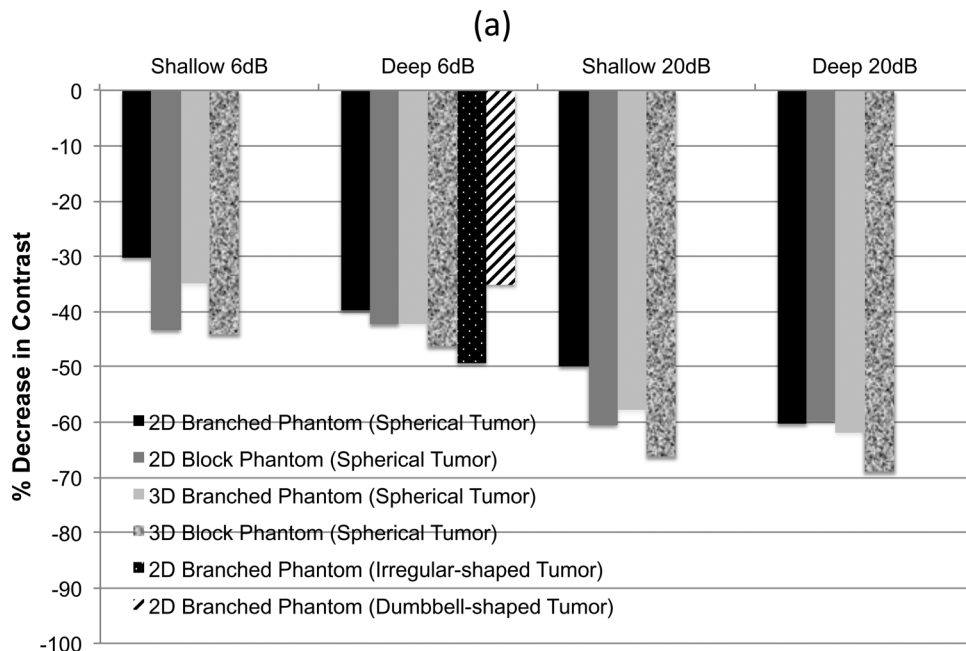


FIG. 15. % decrease in contrast by measuring strain instead of modulus

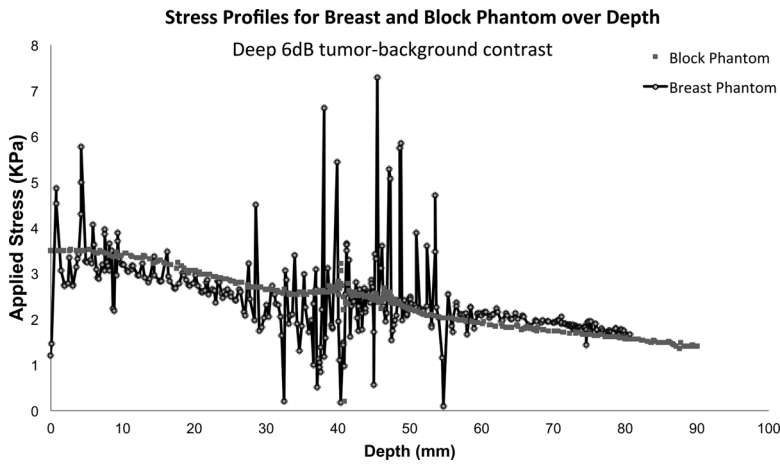


FIG. 16. Variation in normal axial stress over depth for the breast and block phantom for a tumor in a deep location with 6 dB input tumor-background modulus contrast.

From these observations, the branched breast phantom performs better in transferring contrast from modulus to strain. The phantom also allows for differentiation in performance for deep and shallow tumors like what has been seen clinically.²⁶ Deep breast tumors were more difficult to image than shallow tumors. We hypothesize that the branches in the breast phantom offer a way to concentrate the applied stress, which is not done in the block phantom. This helps to achieve better strain contrast. Figure 16 shows a profile of the stress over depth for both the branched breast and the block phantom. We can clearly see stress concentration or elevation at several points along depth due to the glandular structures present in this phantom. No such effect is seen with the block phantom. Increasing in stiffness from 6 dB input tumor-background modulus contrast to 20 dB sig-

nificantly caused a loss in contrast and a much worsened CTE. This effect has been previously reported by Kallel *et al.*¹⁸ and Ponnekanti *et al.*¹⁹ where modulus measurements of low stiffness tumors translated well into their corresponding strain values. As the tumor gets stiffer, stress concentration effects increase around the boundaries of the tumor, resulting in a decrease in stress inside of the tumor. This results in increased strain for the same modulus value. When mapping this new value of strain back to modulus, a lower value of modulus is predicted resulting in a loss of contrast transfer. There is also a loss of contrast for less-stiff tumors but not as severe.

While simulating the phantoms in 3D, the loss of contrast was higher in both branched and block phantoms compared to their 2D counter-parts. This loss of modulus-strain

Axial Strain Maps for Breast Phantom with 3 Types of Tumor Shapes Positioned Deep for 6dB Tumor-Background Contrast

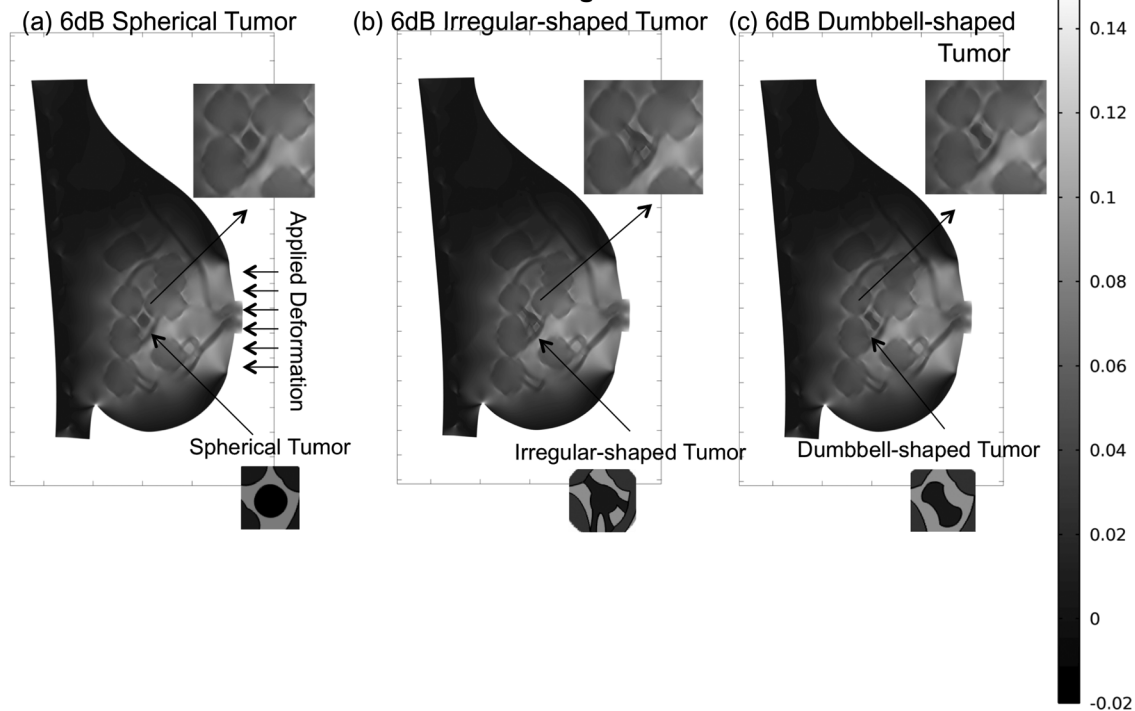


FIG. 17. 2D Normal axial strain image of the breast phantom for a (a) spherical tumor; (b) irregular tumor; and (c) dumbbell tumor in a deep location with 6 dB input tumor-background modulus contrast. Zoomed strain images around the tumor along with the actual shape of the tumor are shown.

contrast in 3D is due to no approximations being used during the simulation, where all components of the strain tensor were allowed to develop. Figure 13 shows 3D normal axial strains mapped with this breast model for a shallow spherical tumor with 6 dB and 20 dB input tumor-background modulus contrast. The use of the plane strain approximation for the 2D case causes an overestimated CTE value compared with the true CTE achieved with the 3D model. Thus, the use of 3D phantoms, like the branched breast phantom, with no approximations will assist in more accurate estimation of modulus, especially valuable with 3D *elastography* systems.

Finally, the CTE predicted with irregular shaped tumors was the worst. Such a behavior of loss of contrast has been seen clinically as well; where spherical shaped benign tumors are easier to visualize than irregular shaped malignant cancers. Figure 17 shows 2D strain results for the breast phantom for three shapes of tumors— spherical, dumbbell, and irregular shaped. We can see that the spherical and dumbbell tumor show clearer boundary effects than the irregular tumor.

VI. CONCLUSIONS

We have developed a novel 3D breast software phantom that uses a commercial mechanical design tool instead of using mathematical equations or real-imaging data, as proposed by others. We illustrate its use in simulating *elastography* using biomechanical FEM modeling. The model uses several illustrations of breast anatomy to guide the shape of the breast, dimensions of the ductal structure, and relative proportions of tissue types (glandular, fat, and muscle). Once the breast phantom is established, modifications are fairly simple. The anatomy/geometry of the breast can be modified in SOLIDWORKS, the design tool, and the biomechanics associated with *elastography* can be modified in the FEM tool, COMSOL. For instance, the breast shape, size, shape, and location of tumors, ratio of glandular to fatty content, ductal structure (ductal branches, lobes, and lobules), etc., can be fairly easily modified by a student/researcher familiar with SOLIDWORKS or AUTOCAD. Biomechanical parameters in COMSOL can be changed once the breast software phantom is imported. For instance, changes in mechanical properties, loading conditions, linear/nonlinear modeling scenarios, elastic/viscoelastic modeling, multiphysics modeling, etc., can be easily done, by a researcher familiar with FEM modeling.

One of the first steps in biomechanical modeling was meshing the geometry. We used residual modulus maps and profiles as a guide to help optimize the mesh for this complex geometry, by starting with an initial guess for the mesh and subsequent tweaking to reduce overall residual modulus. The mesh with the least residual modulus that achieved convergence was chosen as the optimal mesh. Once meshing was achieved and other biomechanical parameters were defined, a 4 N force was applied on the surface of the breast just above the tumor with the shape of the load boundary chosen to mimic a linear array transducer commonly used in clinical *elastography*. Strains of around 5% in the background glandular region were measured for a 4 N force, simi-

lar to what was measured in a clinical *elastography* study with the same force.⁴¹

From our FEM analysis of *elastography*, the breast phantom offered important advantages over traditional block phantoms commonly used. It offered a superior CTE or decreased loss of contrast from modulus to strain in both 2D with plane strain approximations and in 3D with no approximations. The breast phantom showed differences in CTE values and strain contrast for deep and shallow tumors, like what has been seen clinically.²⁶ The breast phantom also showed significant change in CTE when 3D modeling was used, when all components of the strain tensor were allowed to develop, over 2D plane strain modeling. Such a prominent change was not seen in the block phantom. Finally, the phantom has a more realistic 3D shape, size, and internal structure. Like the traditional block phantom, the breast phantom also showed worsened CTE values when the input tumor-background modulus contrast was increased from 6 dB to 20 dB. The irregular tumor showed the worst CTE values when compared to the spherical and the dumbbell shaped tumors. Both phantoms allowed for 2D vs 3D simulations to assess CTE differences under plane strain approximations.

We hypothesize that improvements in the performance of the breast phantom are due to the ductal branches that offer a way to concentrate the applied stress, which is not done in the block phantom. This helps to achieve better strain contrast. Furthermore, the use of the plane strain approximation for the 2D case causes an overestimated CTE value compared with the true CTE achieved with the 3D model. Using displacements and strains from the 2D case for the purposes of modulus reconstruction will affect the accuracy of the estimates. Hence, the use of 3D phantoms with 3D strains and displacements will offer more accurate estimates of modulus—particularly important with growing interest in 3D *elastography* systems.

We also recognize some important limitations and avenues for future work with this software breast phantom from a design perspective and with simulating *elastography*. First, the 3D design model can be made as detail as possible in its structure but becomes limited by the ability to mesh the structure. Second, our comparison in this paper is limited to a commonly used *elastography* phantom, a simple rectangular phantom with spherical inclusion. We have not compared this to other mathematical or voxelized phantoms as creation of these types of phantoms are challenging and warrant separate studies. It is currently unclear if these types of phantoms will outperform this breast phantom. Third, our parametric study is limited to tumor shape, stiffness, and location with 2D or 3D modeling. It is possible to vary other parameters of the breast geometry and biomechanics, like location of force or magnitude and type of applied force, to look for conditions where maximum sensitivity of the technique can be achieved. This will be a topic for future research. Fourth, we limit our modeling technique to linear modeling with small finite deformations. We understand that clinical *elastography* sometimes involves large deformations used to exploit the hyperelasticity of the tissue for increased contrast. The current model/solver used in this study is incapable of doing

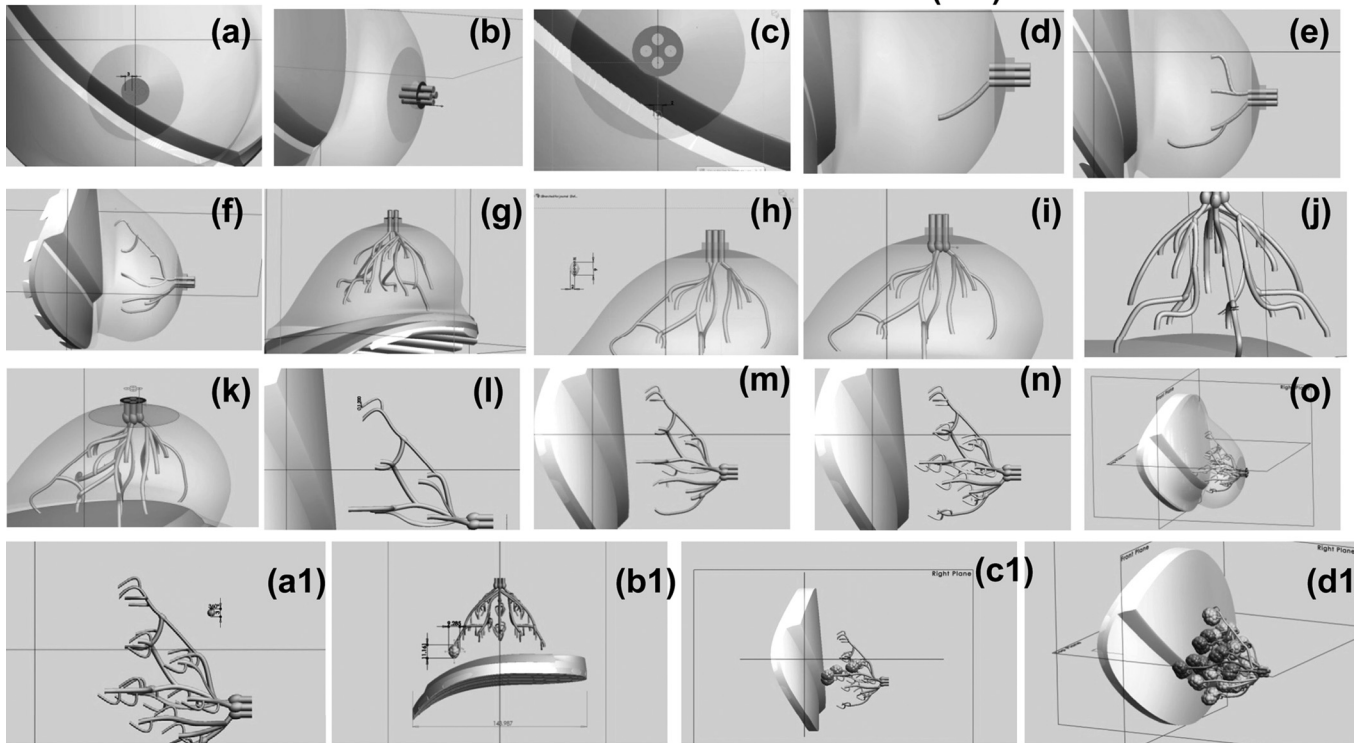
this. We are currently pursuing nonlinear modeling as an alternative to explore these effects. Optimization of these nonlinear solver parameters is nontrivial and will form a separate work. Fifth, our choice of material properties is limited by *ex vivo* measurements and this affects the realism of the model. However, we are limited by this data for our models. Further, other works on breast biomechanical modeling for applications like mammography have made similar choices. Sixth, our current study is limited to CTE testing only and does not explore any modulus reconstruction. We concentrate on reporting the design of this novel breast phantom and its basic use in the field of *elastography*. Other applications, like modulus reconstruction will be a topic for future research.

In conclusion, in terms of usefulness of this breast model for elastography, the framework is—(a) flexible in both, the choice of the breast geometry (breast shape, contours, glandular/fat content, tumor size, shape, and location) and biomechanical parameters (gravitational load, location of stress, stress profile, solvers, etc.) to allow for simulation of elastography in areas of CTE testing, non-linear/linear modeling, hyperelasticity/viscoelasticity, and modulus reconstruction. We illustrate CTE testing with linear modeling in this paper.

(b) It has a more realistic 3D shape, size and internal structure when compared to simple phantoms and can serve as an intermediate assessment tool between these simple phantoms and actual patients for investigation of elastography. (c) It out-performs simple phantoms in terms of contrast transfer efficiency in both 2D and 3D simulations and showed differences in contrast and CTE values for deep and shallow tumors, like what has been seen clinically. Contrast from simple phantoms did not vary with depth. We hypothesize that the ductal branches offer a way to concentrate the applied stress, which is not done in the simple phantoms. This helps to achieve better strain contrast. (d) The phantom can be modeled using hyperelastic parameters of breast to simulate scenarios of large compressions commonly seen in clinic, which will be a subject of future work. A maximum sensitivity analysis will be then conducted to determine best compression level, compression rate, and preload to visualize best strain contrast and CTE for tumors of different shapes, sizes, location, and stiffness.

Such information will be extremely useful to guide clinicians in applying the right stress profile to maximize contrast to possibly obviate difficulties in imaging small, deep, less

Creation of the Ductal Branches (a-o)



Creation of Lobules and Tumor (a1-f1)

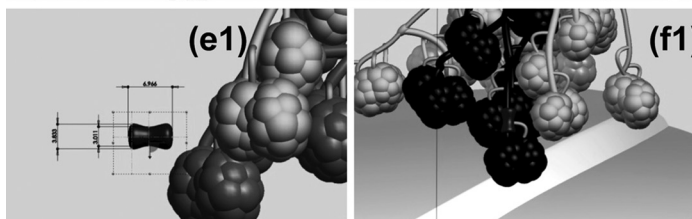


FIG. 18. Step by step illustration of the creation of the ductal branches, lobules, and tumor.

stiff tumors. In the current work, the stress profile was kept constant and comparisons were made between this phantom and a simple rectangular phantom for different tumor stiffness, shape, and location to introduce this phantom into the field of elastography.

APPENDIX A: DETAILED FIGURES FOR BREAST PHANTOM CREATION

In this appendix, we describe the process of the breast phantom creation in detail primarily for the creation of ductal branches and lobes/lobules. We have omitted details for muscle and breast boundary creation due to lack of space. However, the process is very similar to the others that are included here.

Ductal branches creation

- Create sketch (sk-10) parallel to the coronal plane of the breast [Fig. 18(a)].
- Using the Solid Sweep tool, extrude these ducts through the nipple into the fat region [Fig. 18(b)].
- Create another sketch (sk-11) 6 mm below the lower most duct parallel to the front plane, at a distance of 13 mm into the fat region from the edge of the lower most duct [Fig. 18(c)].
- Define a profile path from the center of the sketch (sk-11) to the edge of the lower most duct [Fig. 18(d)].
- Using the Solid Sweep tool, create another duct by sweeping sketch (sk-11) along the profile defined [Fig. 18(e)].
- In the same manner, i.e., by defining a sketch for duct diameter and a profile path for the sweep and using Solid Sweep tool to create solid ducts, further create more ducts in an arbitrary manner [Figs. 18(f) and 18(g)].
- Define a sketch (sk-12) and convert it into a solid ellipsoid [Fig. 18(h)].
- Using Move/Copy tool, copy this ellipsoid on top of the ducts, just below the nipple [Fig. 18(i)].
- For the purpose of making ductal structure smoother wherever necessary copy and place the ellipsoids where different ducts intersect and scale them to the desired size [Fig. 18(j)].
- Using Surface Cut tool, delete the portions of ducts that protrude out of the breast [Fig. 18(k)].
- Following the procedure in step 6, create terminating branches [Fig. 18(l)].
- Using Scale and Move/Copy tools, replicate the ducts created in step 11 and place them at the end of ducts created in step-6 [Figs. 18(m) and 18(n)].
- Using the Combine tool, merge all the ducts into a single solid body [Fig. 18(o)].

Lobules and tumor creation

- Using Solid Revolve tool, create a sphere of 3 mm in diameter representing a single lobule (Fig. 18(a1)).
Using Copy/Move tool, make multiple copies of this lobule and stack them together in the form of a lobe [Fig. 18(b1)].

- Using the combine tool, merge all the individual lobules in the lobe into a single body.
- Using Copy/Move tool, create multiple copies of the lobe and place them at the end of every terminating branch [Figs. 18(c1) and 18(d1)].
Using the Scale tool, resize lobes to introduce variability in the model. Final ductal structure is shown in Fig. 18(e1).
- Figure 18(e1) shows an example of a dumbbell shaped tumor. Using Copy/Move tool place it in one of the terminating ducts [Fig. 18(f1)].

^{a)}Author to whom correspondence should be addressed. Electronic mail: s.naema@gmail.com

^{b)}Electronic mail: mallika.keralapura@sjsu.edu

¹C. Zygantidis and K. Bliznakova, "A novel simulation algorithm for soft tissue compression," *Med. Biol. Eng. Comput.* **45**, 661–669 (2007).

²V. Rajagopal, P. M. F. Nielsen, and M. P. Nash, "Modeling breast biomechanics for multi-modal image analysis successes and challenges," *WIREs Syst. Biol. Med.* **2**, 293–304 (2010).

³F. Lefebvre, H. Benali, R. Gilles, and D. Paola, "A simulation model of clustered breast microcalcifications," *Med. Phys.* **21**, 1865–1874 (1994).

⁴D. Lazos, Z. Kolitsi, and N. Pallikarakis, "A software data generator for radiographic imaging investigations," *IEEE Trans. Inf. Technol. Biomed.* **4**, 76–79 (2000).

⁵J. Nappi, J. Dean, O. Nevalainen, and S. Toikkanen, "Algorithmic 3D simulation of breast calcifications for digital mammography," *Comput Methods Biomed Res.* **66**, 115–124 (2001).

⁶P. R. Bakic, M. Albert, and A. D. A. Maidment, "Mammogram synthesis using a 3D simulation. I. Breast tissue model and image acquisition simulation," *Med. Phys.* **29**, 2131–2140 (2002).

⁷K. Bliznakova, Z. Bliznakov, V. Bravou, Z. Kolitsi, and N. Pallikarakis, "A 3D breast software phantom for mammography simulation," *Phys. Med. Biol.* **48**, 3699–3721 (2003).

⁸A. Samani, M. Yaffe, and D. Plewes, "Biomechanical 3D finite element modelling of the human breast using MRI data," *IEEE Trans. Med. Imaging*, **20**, 271–279 (2001).

⁹C. M. Li, W. P. Segars, G. D. Tourassi, J. M. Boone, and J. T. Dobbins, "Methodology for generating a 3d computerized breast phantom from empirical data," *Med. Phys.* **36**(7), 3122–3131 (2009).

¹⁰C. Hoeschen, U. Fill, M. Zank, W. Panzer, D. Regulla, and W. Dhring, "A high-resolution voxel phantom of the breast for dose calculations in mammography," *Radiat. Prot. Dosim.* **14**, 406–409 (2005).

¹¹F. Azar, D. Metaxas, and M. Schnall, "A deformable finite element model of the breast for predicting mechanical deformations under external perturbations," *Acad. Radiol.* **8**, 965–975 (2001).

¹²N. Ruiters, R. Stotzka, T. O. Muller, H. Gemmeke, and J. R. Reichenbach, "Model-based registration of x-ray mammograms and MR images of the female breast," *IEEE Trans. Nucl. Sci.* **53**, 204–211 (2006).

¹³D. Palomar, B. Calvo, J. Herrero, J. Lopez, and M. Doblare, "A finite element model to accurately predict real deformations of the breast," *Med. Eng. Phys.* **30**, 1089–1097 (2008).

¹⁴P. Pathmanathan, D. J. Gavaghan, J. P. Whiteley, S. J. Chapman, and J. M. Brady, "Predicting tumor location by modelling the deformation of the breast," *IEEE Trans. Biomed. Eng.* **55**, 2471–2480 (2008).

¹⁵V. Rajagopal, A. Lee, J. Chung, R. Warren, and R. P. Highnam, "Creating individual-specific biomechanical models of the breast for medical image analysis," *Acad. Radiol.* **15**, 1425–1436 (2008).

¹⁶J. Ophir, I. Cespedes, H. Ponnekanti, Y. Yazdi, and X. Li, "Elastography: A qualitative method for imaging the elasticity of the biological tissues," *Ultrason. Imaging* **13**, 111–134 (1991).

¹⁷M. S. Richards, A. A. Oberai, and P. E. Barbone, "Quantitative three-dimensional elasticity imaging from quasi-static deformation: A phantom study," *Phys. Med. Biol.* **54**, 757–779 (2009).

¹⁸F. Kallel, M. Bertrand, and J. Ophir, "Fundamental limitations on the contrast-transfer efficiency in elastography: An analytic study," *Ultrasound Med. Biol.* **22**(4), 463–470 (1996).

¹⁹H. Ponnekanti, J. Ophir, Y. Huang, and I. Cespedes, "Fundamental mechanical limitations on the visualization of elasticity contrast in elastography," *Ultrasound Med. Biol.* **21**, 533–543 (1995).

- ²⁰J. P. Whiteley and D. J. Gavaghan, "Non-linear modeling of breast tissue," *Math. Med. Biol.* **24**, 327–345 (2007).
- ²¹Y. Zhu, T. J. Hall, and J. Jiang, "A finite-element approach for Young's modulus reconstruction," *IEEE Trans. Med. Imaging* **22**(7), 890–901 (2003).
- ²²A. A. Oberai, N. H. Gokhale, S. Goenezen, P. E. Barbone, T. J. Hall, A. M. Sommer, and J. Jiang, "Linear and nonlinear elasticity imaging of soft tissue in vivo: Demonstration of feasibility," *Phys. Med. Biol.* **54**(5), 1191–1207 (2009).
- ²³B. S. Garra, E. I. Cespedes, J. Ophir, S. R. Spratt, R. A. Zuurbier, C. M. Magnant, and M. F. Pennanen, "Elastography of breast lesions: Initial clinical results," *Radiology* **202**, 79–86 (1997).
- ²⁴T. J. Hall, Y. Zhu, and C. S. Spalding, "In vivo real-time freehand palpation imaging," *Ultrasound Med. Biol.* **29**, 427–435 (2003).
- ²⁵D. M. Regner, "Breast lesions: Evaluation with us strain imaging clinical experience of multiple observers," *Radiology* **238**, 425–437 (2006).
- ²⁶H. Zhi, X. Xiao, H. Yang, B. Ou, and Y. Wen, "Ultrasonic elastography in breast cancer diagnosis: Strain ratio vs 5-point scale," *Acad. Radiol.* **17**, 1227–1233 (2010).
- ²⁷R. G. Barr, "Real-time ultrasound elasticity of the breast: Initial clinical results," *Ultrasound*, **26**, 61–66 (2010).
- ²⁸Y. Qiu, M. Sridhar, J. K. Tsou, K. K. Lindfors, and M. F. Insana, "Ultrasonic viscoelasticity imaging of nonpalpable breast tumors: Preliminary results," *Acad. Radiol.* **15**, 1526–1533 (2008).
- ²⁹E. L. Madsen, M. A. Hobson, G. R. Frank, H. Shi, J. Jiang, T. J. Hall, T. Varghese, M. M. Doyley, and J. B. Weaver, "Anthropomorphic breast phantoms for testing elastography systems," *Ultrasound Med. Biol.* **32**(6), 857–874 (2006).
- ³⁰M. Schunke, L. M. Ross, and E. D. Lamperti, *Thieme Atlas of Anatomy: General Anatomy and Musculoskeletal System* (Thieme Medical Publishers, New York, 2005).
- ³¹A. Gefen and B. Dilmoney, "Mechanics of the normal woman's breast," *Technol. Health Care* **15**, 259–271 (2007).
- ³²A. P. Cooper, *Anatomy of the Breast* (Orme, Green, Browne and Longmans, London, 1840).
- ³³D. T. Geddes, "Inside the lactating breast: The latest anatomy research," *J. Midwifery Womens Health* **52**(6), 501–506 (2007).
- ³⁴D. T. Ramsay, J. C. Kent, R. A. Hartmann, and P. E. Hartmann, "Anatomy of the lactating human breast redefined with ultrasound imaging," *J. Anat.* **206**, 525–534 (2005).
- ³⁵M. J. Gooding, J. Finlay, J. A. Shipley, M. Halliwell, and F. A. Duck, "Three-dimensional ultrasound imaging of mammary ducts in lactating women: A feasibility study," *J. Ultrasound Med.* **29**, 95–103 (2010).
- ³⁶N. A. Lee, H. Rusinek, J. Weinreb, R. Chandra, H. Toth, C. Singer, and G. Newstead, "Fatty and fibroglandular tissue volumes in the breasts of women 20–83 years old: Comparison of x-ray mammography and computer-assisted MR imaging," *Am. J. Roentgenol.* **168**, 501–506 (1997).
- ³⁷F. H. Netter, *Atlas of Human Anatomy*, 4th ed. (Elsevier, New York, 2006).
- ³⁸B. Strauch and H.-L. Yu, *Atlas of Microvascular Surgery: Anatomy and Operative Techniques* (Thieme Medical Publishers, New York, 2006).
- ³⁹E. Abrams, M. Mohr, C. Engel, and M. Bottlang, *Cross-sectional Geometry of Human Ribs*, (Biomechanics Laboratory, Legacy Clinical Research and Technology Center, Portland, OR).
- ⁴⁰H. T. Liu, L. Z. Sun, G. Wang, and M. W. Vannier, "Analytic modeling of breast elastography," *Med. Phys.* **30**(9), 2340–2349 (2003).
- ⁴¹M. Sridhar and M. F. Insana, "Ultrasound measurements of breast viscoelasticity," *Med. Phys.* **54**, 4757–4767 (2007).
- ⁴²A. Thitaikumar, L. M. Mobbs, C. M. Kraemer-Chant, B. S. Garra, J. Ophir, "Breast tumor classification using axial shear strain elastography: A feasibility study," *Phys. Med. Biol.* **53**, 4809–4823 (2008).
- ⁴³S. Timoshenko, *Theory of Elasticity* (McGraw-Hill, New York, 1970).
- ⁴⁴T. A. Krouskop, T. M. Wheeler, F. Kallel, B. S. Garra, and T. Hall, "The elastic moduli of breast and prostate tissues under compression," *Ultrasound Imaging* **20**, 260–274 (1998).
- ⁴⁵P. S. Wellman, R. D. Howe, E. Dalton, and K. A. Kern, *Breast Tissue Stiffness in Compression is Correlated to Histological Diagnosis* (Harvard BioRobotics Laboratory, Division of Engineering and Applied Sciences, Harvard University, Harvard, 1999).
- ⁴⁶T. Shih, J. Chen, D. Liu, K. Nie, L. Sun, M. Lin, D. Chang, O. Nalcioglu, and M. Su, "Computational simulation of breast compression based on segmented breast and fibroglandular tissues on magnetic resonance images," *Phys. Med. Biol.* **55**, 4153–4168 (2010).
- ⁴⁷V. Rajgopal, A. Lee, J. Chung, R. Warren, R. Highnam, P. M. F. Nielsen, and M. P. Nash, "Towards tracking breast cancer across medical images using subject specific biomechanical models," *MICCAI, LNCS*, Vol. 4791, pp. 651–658 (2007).
- ⁴⁸E. Y. K. Ng, W. K. Ng, L. S. J. Sim, and U. R. Acharya, "Numerical modeling of biopotential fields for detection of breast tumors," *Comput. Biol. Med.* **37**(8), 1121–1132 (2007).
- ⁴⁹S. C. Tadepalli, A. Erdemir, and P. R. Cavanagh, "Comparison of hexahedral and tetrahedral elements in finite element analysis of the foot and footwear," *J. Biomech.* **44**(12), 2337–2343 (2011).
- ⁵⁰G. Chen, B. Schmutz, D. Epari, K. Rathnayaka, S. Ibrahim, M. A. Schuetz, and M. J. Pearcy, "A new approach for assigning bone material properties from CT images into finite element models," *J. Biomech.* **43**(5), 1011–1015 (2010).